Investigating the phase behaviour of binary suspensions of cellulose nanocrystals and montmorillonite with nonlinear rheology, SAXS and polarized optical microscopy

Catherine Tom, Erwan Paineau, Ravi Kumar Pujala

Investigating the phase behaviour of binary suspensions of cellulose nanocrystals and montmorillonite with nonlinear rheology, SAXS and polarized optical microscopy

Catherine Tom[a], Erwan Paineau[b] and Ravi Kumar Pujala[a,b]*

[a]*Soft and Active Matter group, Department of Physics and Centre for Atomic, Molecular and Optical Sciences & Technologies (CAMOST), Indian Institute of Science Education and Research (IISER) Tirupati, Andhra Pradesh, 517507, India*

[b]*Université Paris-Saclay, CNRS, Laboratoire de Physique des Solides, Orsay 91405, France*

Corresponding author E-mail address: *pujalaravikumar@iisertirupati.ac.in*

Abstract

Using microscopy imaging techniques, X-ray scattering, and nonlinear rheological measurements, we have examined microstructural changes, and phase behavior of cellulose nanocrystals (CNC)/montmorillonite (MMT) composite colloidal systems. Fourier-transform (FT) rheology-stress decomposition methods, Lissajous-Bowditch plots, and other techniques are used to both qualitatively and quantitatively determine the various phases that the suspensions exhibit. In the MAOS (medium amplitude oscillatory shear) region, multiple scaling regions, as well as quadratic scaling regions are obtained. The dependence of the normalized third relative intensity ($I_{3/1}$) values on angular frequency (ω) also provided new insights into how nonlinear parameters depend on the various CNC/MMT phases. These findings allow us to differentiate various phases exhibited by the composite system, including the isotropic, biphasic, and chiral nematic liquid crystalline (LC) phases. The CNC/MMT nanocomposite system exhibits a variety of liquid crystalline phases, which may contribute to improved mechanical properties for the system, including increased mixture strength, stiffness, and toughness because of the particle alignment in the LC phase. Additionally, the field of optics and photonics may find use for this nanocomposite system in the fabrication of sensors, polarizers, and optical films; energy storage applications where the aligned structures facilitate ion transport; and the formulation of paints and coatings where the strain stiffening and shear thinning behavior of the CNC/MMT composite system are critical.

Keywords Cellulose nanocrystals · Rheology · CNC/Montmorillonite nanocomposite · Large amplitude oscillatory shear (LAOS) · Strain stiffening · Lissajous-Bowditch plots

1. Introduction

Due to their ubiquitous ability to display a wide variety of phase states with captivating macroscopic properties, colloidal suspensions are of great interest. Transitions between these phase states are permitted when applying stresses or deformations, changing the chemical composition, or both [1]. Inter-particle interactions play a crucial role in determining the macroscopic behavior of a suspension as the concentration of colloidal particles increases. This can ultimately result in the formation of distinct phase states, such as gel [2,3], glass [2,4], liquid crystals [5–8] or viscoelastic fluids [9,10]. To comprehend the stability, gelation, and aggregation behavior of the colloids that are significant to the food [11,12], pharmaceutical [13] and cosmetic [14] industries, it is imperative to comprehend their microstructural and rheological characteristics. Colloidal suspensions exhibit fascinating transitions between liquid, gel, and liquid crystalline phases that have been the subject of decades' worth of research and study. These phase transitions in complex fluids can be investigated using a variety of techniques, such as imaging and scattering methods. Neutron scattering method is one such technique to probe the internal structure and phase transitions happening in complex fluids [15–17]. Characterization of nanocellulose and the structural details of the modified CNCs has been revealed by Small angle neutron scattering (SANS) technique [18–20]. In order to determine the phase behaviors and microstructural changes occurring in the systems under deformation, rheological measurements are also crucial. The large amplitude oscillatory shear (LAOS) test is crucial in this regard since it is one of the primary techniques used to identify the phase behaviors and microstructural modifications exhibited by complex fluids. During processing, the polymeric materials used in biological and industrial applications must experience rapid deformations. Nonlinear tests (LAOS) are required to simulate the large deformations on these materials because the small amplitude (linear) oscillatory shear tests (SAOS) used to measure the viscoelastic properties of samples would be insufficient in this situation [21,22]. A non-sinusoidal stress response is observed in this instance, corresponding to a sinusoidal input strain. The degree of nonlinearity observed can be quantified through the application of Fourier transform (FT) rheology [23–25], stress decomposition techniques [26,27] Lissajous-Bowditch plots [28] and Chebyshev polynomials [23].

The polymer derivative of cellulose called cellulose nanocrystals (CNC) has special qualities that make them appealing, like a large aspect ratio, surface area, biodegradability, and self-assembly behavior.

Because of these advantageous qualities, CNC has become one of the most promising materials among other solid stabilizers for use in Pickering emulsions [29]. In order to control the dispersion of droplets within formulations, Saidane et al. investigated changing the surface chemistry of CNCs for emulsion processing and were able to create functional emulsions without the need of surfactants [30]. The morphology (size and shape) of the CNC, surface charge [31,32], wettability [33,34], and crystalline allomorph of CNC [35] affect how well it performs in the emulsification process [36].

At higher concentrations, as in the case of cellulose microfibrils, these nanoparticles self-assemble to form different liquid crystalline phases because of the large aspect ratio of CNC [37–39]. Shafiei et al. have used polarized optical microscopy imaging techniques and rheological studies to investigate the microstructural and rheological characteristics of nanocrystalline cellulose [40–42]. The fingerprint texture from polarized optical microscopy (POM) imaging techniques confirms that at higher concentrations, nanocrystalline cellulose exhibits a transition from isotropic to chiral nematic liquid crystalline phase [40,43,44]. At higher concentrations, the presence of a liquid crystalline phase in CNC suspensions was also demonstrated by the three-region viscosity profile obtained from rheological observations [40,43–45]. Using LAOS measurements, Wojno et al. investigated the phase transitions and microstructural changes occurring to the system. Since different liquid crystalline phases displayed by CNC suspensions could not be distinguished by the viscosity profile derived from linear rheological measurements, LAOS could offer this information through its FT rheology and stress decomposition techniques. Rheo-PLI experiments could be used to determine the impact of various CNC phases on the nonlinear parameters [46]. Wojno et al. postulated that the various phases displayed by CNC aqueous suspensions could be explained by the dependence of the nonlinear parameter $I_{3/1}$ on angular frequency ω and the multiple scaling regions observed on the $I_{3/1}$ vs shear strain plot in the middle amplitude oscillatory shear region (MAOS) and LAOS. When the concentration rises above 5 w/v%, pure CNC aqueous suspensions exhibit a complete liquid crystalline phase as they show quadratic scaling in the MAOS region [46].

The viscoelastic properties of the CNC/composite systems have been improved by a variety of additives added to CNC aqueous suspensions [47–52]. Its gelation qualities have improved with the addition of inorganic clay materials, and it may be utilized to create functional nanocomposites [3,53–56]. In order to improve the elastic modulus and viscosity of CNC aqueous suspensions, Laponite, a synthetic inorganic clay with a disc-shaped morphology,

has been added [3]. It has also been used as a model binary system to examine the intricate relationships between 1D and 2D systems. Research on CNC/clay systems is crucial because the binary mixture may be utilized to create functional nanocomposites and the clay minerals may improve the gelation behavior of pure CNC aqueous suspensions. The naturally occurring inorganic clay mineral montmorillonite (MMT) has a diameter of 250 nm and a plate-like morphology [57,58]. MMT could readily form interactions with CNC particles because of its shape and charge anisotropy, which would improve the viscoelastic properties of the CNC/MMT composite system [54,59,60]. The identification of different phases exhibited by CNC/composite systems using LAOS measurements is still in its infancy, despite the fact that numerous studies on their rheological behavior have been conducted thus far. The present study has used LAOS measurements to systematically investigate the phase behaviors displayed by CNC/Montmorillonite (MMT) systems as well as the microstructural changes during deformation. The MITlaos framework, a MATLAB version designed to characterize nonlinear viscoelasticity, facilitates the analysis of LAOS data and makes it possible to identify the intra-cycle nonlinearities that the CNC-MMT suspensions exhibit, such as strain softening/stiffening and shear thickening/thinning behavior. The microstructural changes, and phase behavior of cellulose nanocrystals (CNC)/montmorillonite (MMT) composite colloidal systems have been investigated in detail using microscopy imaging techniques, X-ray scattering, and nonlinear rheological measurements. Many improvements could be made in a variety of industrial fields by comprehending and adjusting the LC phases as well as the strain stiffening and shear thinning behavior of CNC/MMT composite systems at higher strain amplitudes.

2. Material and methods

2.1. Sample preparation

Na^+-MMT was bought from Southern Clay Products in the US and CNC powder was bought from Celluforce in Canada. Both products were used as originally supplied, requiring no additional processing. CNC particles have a zetapotential of -31.6 mV and a size range of 100-300 nm, while MMT particles have a zetapotential of -37.5 mV and a size range of 250-330 nm, respectively. CNC/MMT composite suspensions were prepared using Milli-Q water as the solvent. The sample solution was stirred with a magnetic stirrer to ensure that all of the particles had dispersed well.

2.2. Optical observations

Using a Panasonic DMC-FZ18 camera, images of CNC/MMT composite samples in 5 ml glass vials were taken between two polaroid sheets that are kept perpendicular to one another (cross polarizers). Using a polarising microscope (Nikon LV100N-POL), the microscopy images were captured both with and without the quarter wavelength retardation plate (λ/4 plate, λ= 546 nm) inserted between the cross polarizers. This plate aids in enhancing the birefringence that is obtained from the preferential orientation of the particle domains.

2.3 X-ray Scattering Experiments

X-ray scattering experiments were performed on the MORPHEUS platform at Laboratoire de Physique des Solides. Small-angle X-ray scattering (SAXS) measurements were carried out on a sealed tube micro source GeniX3D equipped with FOX3D single reflection optics and motorized scatterless slits (Xenocs) delivering a monochromatic beam (λ = 1.542 Å). SAXS patterns were collected on a Pilatus 200K hybrid pixel array detector (pixel size = 172 µm, Dectris Ltd., Switzerland,) placed at a sample-to-detector distance of around 1.7 m. The variation of the scattering intensity (I) with the scattering vector modulus ($Q = 4\pi \sin\theta/\lambda$, where λ is the wavelength and 2θ is the scattering angle) was obtained from azimuthal angular integration of the scattering patterns using standard procedures implemented in Igor software.

2.4. Rheological measurements

Rheological experiments of CNC/MMT composite suspensions were performed on Anton paar MCR 302 rheometer using a cone-plate geometry having a nominal angle of 2^o. Every test was conducted at room temperature. To prevent the solvent from evaporating, the sample was covered with a solvent trap. The samples were subjected to both rotational and oscillatory tests in the linear viscoelastic region.

2.5. Nonlinear rheological measurements

The rheological measurements performed on the nonlinear region to investigate the microstructural changes and phase behaviours of the system are termed Large amplitude oscillatory shear (LAOS) measurements where the strain amplitude γ_0 exceeds the frequency-dependent limit of the material. LAOS measurements were performed using Anton paar MCR 302 rheometer at room temperature. MITlaos framework was used in the analysis of LAOS data. The shear strain used in nonlinear tests ranges from 0.01 to 1000% and the regions could be classified into SAOS (0.01 – 10%), MAOS (10-100%) and LAOS (100-

1000%) regions. FT-rheology stress decomposition method [27] is used to obtain the nonlinear viscoelastic properties of the system at higher deformations quantitatively. The ratio of the third harmonic intensity over the fundamental intensity ($I_{3/1}$) is investigated as it contains the major information about the nonlinearities [22,61]. In the MAOS region, a quadratic scaling of $I_{3/1}$ α γ_0^2 could be observed [22,24,46]. Usually at lower strain amplitudes, the viscoelastic materials exhibit an ellipsoidal shape and a distorted ellipsoidal shape indicates a transition from linear to nonlinear region and the appearance of higher odd harmonics at higher deformations [62–64]. The intra-cycle strain stiffening/softening and shear thickening/thinning behaviours of the composite systems are identified using strain stiffening (S) and shear thickening (T) ratios respectively and are given by equations (1) and (2).

$$S = \frac{G_L' - G_M'}{G_L'} \quad (1)$$

$$T = \frac{\eta_L' - \eta_M'}{\eta_L'} \quad (2)$$

The large strain and minimum strain modulus are represented by G_L' and G_M' respectively. Also η_L' and η_M' are the large shear rate and minimum shear rate viscosities respectively. In the linear viscoelastic region, G_M' = G_L' = G' which implies that both S and T values are zero in the linear regime [65]. The values of $S > 0$ and $S < 0$ indicate strain stiffening and strain softening behaviours respectively. Similarly, for $T > 0$ and $T < 0$, the values indicate the shear thickening and shear thinning behaviour of the suspensions.

3. Results and discussion

3.1. Optical studies

Fig. S1 (Supporting Information) presents polarized optical microscopy images of pure MMT and CNC aqueous suspensions with and without λ/4 plate. The suspensions of MMT are isotropic for all MMT concentrations used in this work (0.1 to 3 w/v%), indicating that no specific LC domains are present in these suspensions. In contrast, at concentrations greater than 3 w/v%, pure suspensions of CNC exhibit birefringent domains (Fig. S1). It is possible to identify the pristine 3 w/v% CNC as an isotropic phase because the POM image displays an entirely dark background and no signs of birefringence [40,66]. Fig. 1 displays polarized optical microscopy images of 3 w/v% CNC with different MMT concentrations.

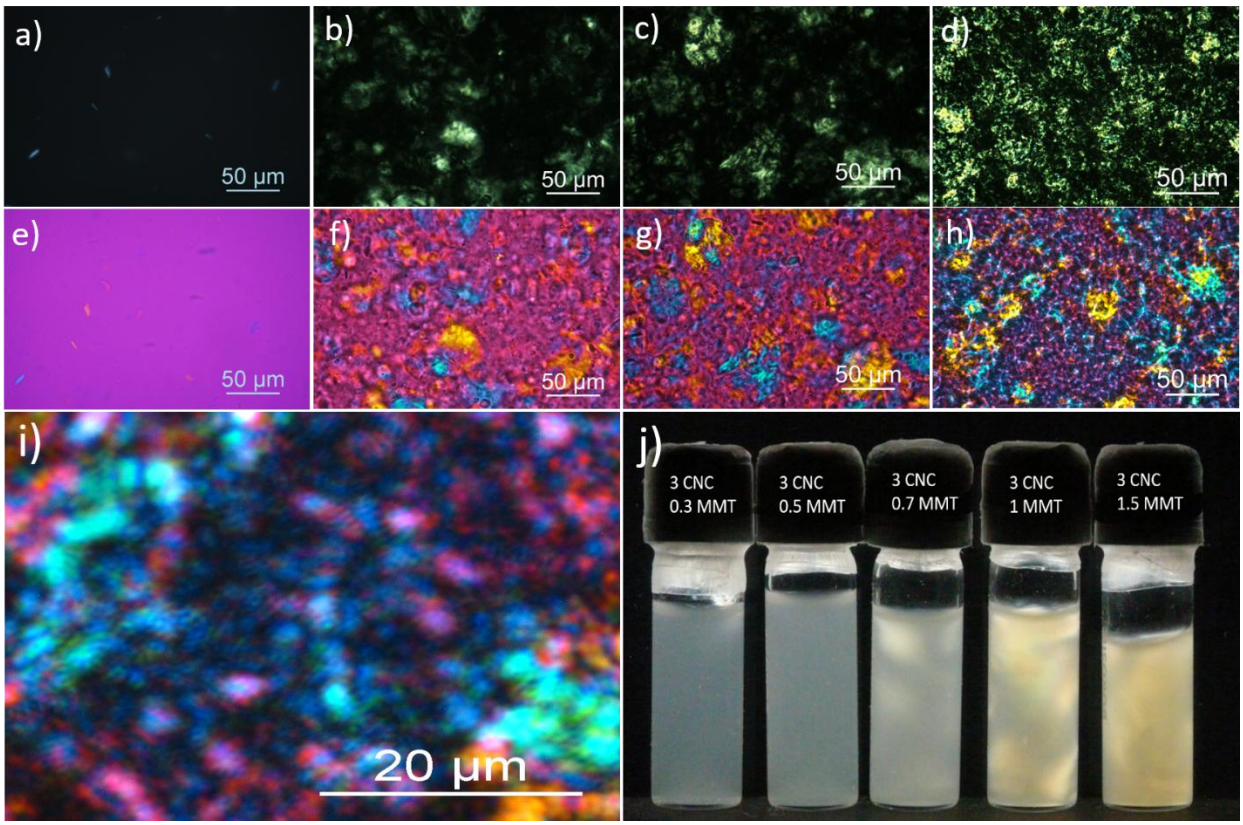

Fig. 1. Polarized optical microscopy images of 3 w/v% CNC with a) 0 b) 0.7 c) 1 and d) 3 w/v % MMT on a glass micro slide covered with a coverslip. POM images obtained by inserting $\lambda/4$ plate between the cross polarizers of 3 w/v% CNC with e) 0 f) 0.7 g) 1 and h) 3 w/v% MMT. i) Enlarged view of the POM images of 3 w/v% CNC with 3 w/v% MMT suspensions with 50X using a $\lambda/4$ retardation plate. j) Visual observations of vials filled with CNC/MMT composite suspensions placed in between cross-polaroid sheets.

When MMT is added to CNC suspensions, birefringent droplets, also known as tactoid, form into the isotropic phase at low concentrations of MMT (0.3 and 0.7 w/v%). We could categorize this as biphasic since it shows the beginning of the liquid crystalline (LC) phase formation in the obtained POM images. A fingerprint pattern is seen when MMT concentration is further raised (1-2 w/v%), suggesting the existence of a chiral nematic LC phase in which each line corresponds to half the pitch of the particles' helical orientation [37]. Fig. 1i displays an enlarged view of the fingerprint patterns found in CNC/MMT systems. The fully spread fingerprint texture on the gel confirms the formation of a fully birefringent gel with chiral nematic texture as the concentration of MMT rises to 3 w/v%. The orientation of the domains with respect to the polarizers can be determined by using the λ/4 retardation plate (Fig. 1). As the concentration of MMT in CNC suspension rises, birefringence is seen to

improve. In the POM images displayed in Fig. 1, the red and blue colors, respectively, denote the alignment of particle domains parallel and perpendicular to the polarization axis. Fig. 1(j) depicts observations of CNC/MMT composite suspensions made with the naked eye between cross-polaroid sheets. The increased concentration of MMT in the CNC suspensions makes birefringence very evident.

3.2. Microstructural investigation

Using Small-Angle X-ray Scattering (SAXS), the impact of MMT incorporation on the structural organization of CNC is investigated. Fig. 2 shows the evolution of the SAXS profiles and compares them with the scattering patterns obtained for suspensions made of pure CNC and MMT. The scattering data of these two pure suspensions were also fitted as shown in Fig. S2. For MMT, a power-law with an exponent of 2 was obtained, in agreement with the two-dimensional feature of the nanoobjects. TEM image of MMT particles having platelet morphology which were characterized in our previous work [57]. In case of CNC, we used an elliptical cylinder model, allowing obtaining the average diameter (23 nm) and length (470 nm) of the scattering objects in good agreement with the previous AFM observations.

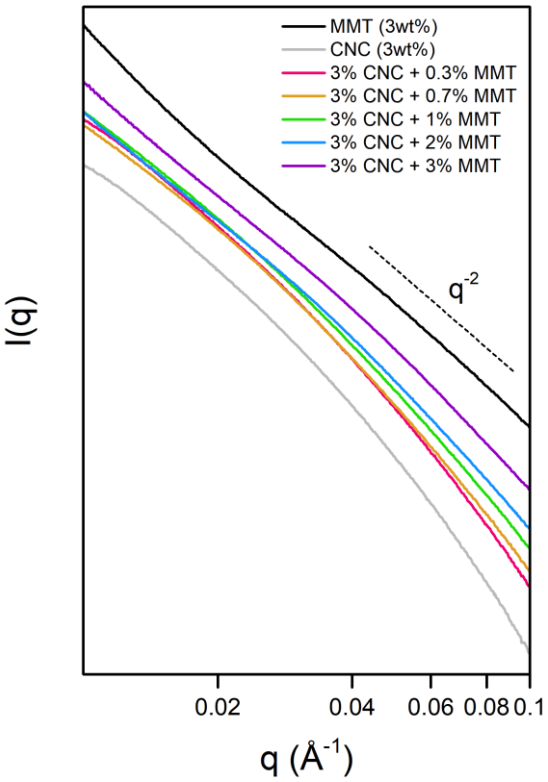

Fig. 2. SAXS profiles for CNC/MMT binary mixtures prepared with 3.0 wt % CNCs and varying concentrations of MMT. The curves have been shifted for the sake of clarity.

For MMT concentration below 1 wt%, the curves are similar to those obtained with CNC suspension. MMT concentration is relatively low to modify the structural organization as observed by optical microscopy (Fig. 1). However, the slope of the SAXS profiles changes progressively with increasing the MMT fraction of the binary suspension to reach a q^{-2} power law dependence for the highest concentration. This exponent relates the bidimensional nature of the scattering objects. This is not very surprising given that the MMT proportions are equivalent to those of the CNCs. The electronic density contrast is therefore dominated by the clay fraction in this q-range. It can also be noted that the evolution of the SAXS profiles with the clay content is different from that previously observed in CNC/Laponite mixtures [3], probably due to the larger size of MMT nanosheets. However, as in the previous study, we are unable to identify any correlation peaks due to short-range positional ordering of the particles for distances lower than 63 nm. In order to gain further insights into the mechanical characteristics of the binary mixtures and the part that the clay particles played, we conducted a thorough rheological characterization.

3.3. Linear oscillatory shear tests

Small amplitude oscillatory shear (SAOS) tests are used to quantify a material's linear rheological response [21]. A sinusoidal stress output is produced corresponding to a sinusoidal strain amplitude as input with a phase angle δ. The storage modulus $G'(\omega)$ and the loss modulus $G''(\omega)$ are the linear rheological material parameters obtained using SAOS tests and are dependent upon the angular frequency ω of deformation alone. Amplitude sweeps, frequency sweeps and flow curves are performed on CNC/MMT samples to investigate the viscoelastic responses on the suspension. Amplitude sweeps were performed with a fixed angular frequency of ω = 1 rad/s and are shown in Fig. 3a. Pristine 3 w/v% CNC suspension shows a liquid behaviour which is evident from the amplitude sweep plots as G'' is dominating over G'. By contrast, the elastic modulus G' is always higher than G'' for all binary suspensions, signifying a gel-like behaviour. There is an increase in the elastic modulus (G') values with concentration of MMT (Fig. S3). At higher concentrations of MMT, G'' suddenly increases at its transition in the nonlinear region and it decreases further showing a weak strain overshoot behaviour. At a concentration of 3 w/v% CNC 1 w/v% MMT onwards weak strain overshoot behaviour is shown by the samples and could be due to the structural network formation taking place between the particles [46,48]. The overshoot in G'' is due to the stronger associations taking place between the particles as a result of an increase in the concentration which leads to the resistance offered by these particle

associations towards restructuring of the samples after larger deformations. The yield stress values are obtained from the amplitude sweep by plotting shear stress versus G' and G'' graph (Fig. S4). The shear stress values corresponding to the limit of linear viscoelastic region are considered as the yield stress values. An increase in the yield stress values corresponding to an increase in the concentration of MMT in CNC aqueous suspension could be observed. Fig. 3b represents the dynamic frequency sweep plot of 3 w/v% CNC with different concentrations of MMT. For pure 3 w/v% CNC, *G''* is dominating over *G'* over the entire investigated frequency range indicating the viscoelastic liquid-like behaviour of the sample. For all other cases, *G'* is dominating over *G''* indicating the gel-like behaviour exhibited by the samples.

The viscosity profiles (Fig. 4a) of the CNC/MMT composite suspensions show that, as the concentration of MMT rises, various phase transitions occur within the system. A shear thinning region and a Newtonian plateau are seen for pristine 3 w/v% CNC suspension. This is a definite indication of the suspension's viscoelastic fluid-like behavior and its transition towards the liquid crystalline phase, where the flow curve displays a three-region profile. It is caused by the alignment of randomly oriented particles along the shear direction.

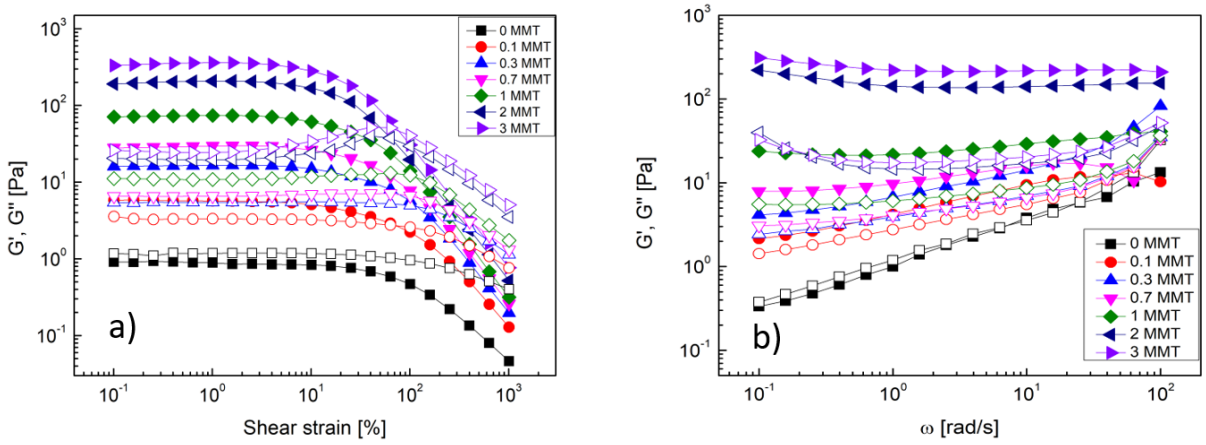

Fig. 3. a) Amplitude sweep and b) frequency sweep of 3 w/v% of CNC with varying concentrations of MMT. Solid and hollow symbols represent the *G'* and *G''* respectively.

When MMT is added to CNC suspensions, a three-region profile is seen. At lower shear rates, this is because the particles are aligned along the shear direction; at mid-shear rate regions, on the other hand, a Newtonian plateau is seen, signifying that all of the particles are aligned along the shear direction and the viscosity stays constant [40,67]. Higher shear rates resulted in the appearance of a shear thinning region once more. This is because the networks

that had formed between the particles broke, causing individual particles to begin aligning along the shear direction. The linear fit of each of the 3 w/v% CNC flow curves at different MMT concentrations is displayed in Fig. S5. Table S1 displays the slopes that resulted from the linear fit of flow curves. The three-region profile of CNC/MMT reveals the liquid crystalline phase exhibited by the composite. Plotted as a function of shear rate in Fig. 4b, the shear stress values increase with the concentration of MMT in CNC aqueous suspension. Herschel Bulkley (HB) model is used to obtain the fitting parameters from the curves and could be described by Equation 3 in which τ and τ_0 represents the shear stress and the yield stress respectively.

$$\tau = \tau_0 + K\dot{\gamma}^n \qquad (3)$$

$K, \dot{\gamma}$ and n represents the consistency factor, shear rate and flow index respectively [68]. Table 1 displays the yield stress values that correspond to various MMT concentrations in CNC/MMT binary mixtures, which were obtained through HB model fitting on shear stress versus shear rate curves. At extremely low to intermediate shear rates, the influence of wall slip becomes predominant, creating challenges in accurately determining the yield stress values. A strong correlation between measurements and HB equation was observed only at higher shear rates [69–71]. With an increase in MMT concentration from 0 to 3 w/v% in aqueous CNC suspensions, yield stress values rise from 0.554 Pa to 68.84 Pa.

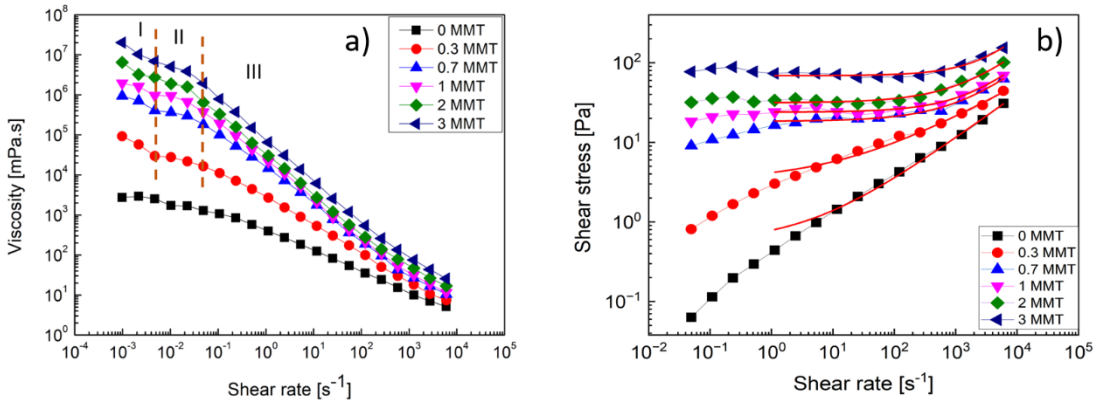

Fig. 4. a) The viscosity profile and b) shear stress versus shear rate plot of 3 w/v% CNC with varying concentrations of MMT. The red line indicates the Herschel Bulkley model fitting on the curves.

Table 1

The parameters derived from the Herschel-Bulkley model fitting shear stress vs. shear rate plot of 3 w/v% CNC at different MMT concentrations.

S. no	Sample	Yield stress [Pa]	*n*	Adj.R^2
1	3 CNC 0 MMT	0.554 ±0.24	0.558±0.01	0.9977
2	3 CNC 0.3 MMT	3.26±0.87	0.435±0.03	0.9903
3	3 CNC 0.7 MMT	18.39±0.07	0.679±0.05	0.9866
4	3 CNC 1 MMT	23.93±0.90	0.745±0.07	0.9796
5	3 CNC 2 MMT	31.41±1.19	0.695±0.05	0.9859
6	3 CNC 3 MMT	68.84±2.20	0.859±0.11	0.9607

Creep tests can be used to obtain the time-dependent viscosity (transient viscosity) evolution. In creep tests, a continuous shear stress is applied in order to measure the transient viscosity. On the viscosity versus time plot, a viscosity bifurcation could be observed around the material's critical shear stress depending on the applied shear stress, whether it is above or below the yield stress of the material [72–74]. We have used shear stresses in the 5–100 Pa range in this work. True yield stress is the shear stress that can be identified in creep tests based on the viscosity bifurcation [68]. The creep tests, which are depicted in Fig. 5, were carried out on 3 w/v% CNC with different MMT concentrations and shear stress applied between 5 and 100 Pa. The creep test results show a distinct viscosity bifurcation around the yield stress value. The transient viscosity in the case of a 3 w/v% pristine CNC suspension decreases over time for all applied shear stresses (5 - 100 Pa). When MMT is added to CNC suspension, the yield stress value rises and, in the case of 3 CNC 0.7 MMT, is between 10 and 20 Pa. The viscosity increases with time below 20 Pa and falls with time above that value, indicating a distinct bifurcation in viscosity. Table 2 lists the yield stress values derived from the creep test. When conducting a creep test, transient viscosity increases if the applied shear stress values are less than the material's yield stress value. This is because microstructural restructuring predominates over its destruction. As the applied shear stress is greater than the material's yield stress, the transient viscosity decreases, suggesting that

microstructure destruction (network breakage) predominates over restructuring. The range of true yield stress values is nearly identical to the values of yield stress obtained using HB model fitting parameters on the shear stress versus shear rate plot (Fig. 4b and Table 1). The rheometer may introduce noise or have limitations in sensitivity which could contribute to data dispersion at shorter time points. The yield stress values increase with an increase in MMT concentration in CNC/MMT binary mixtures. A similar trend of viscosity bifurcation as seen in the case of the transient viscosity versus time plot could be seen here as well and is shown in SI (Fig. S6) when shear strain is plotted as a function of time for CNC/MMT binary mixtures.

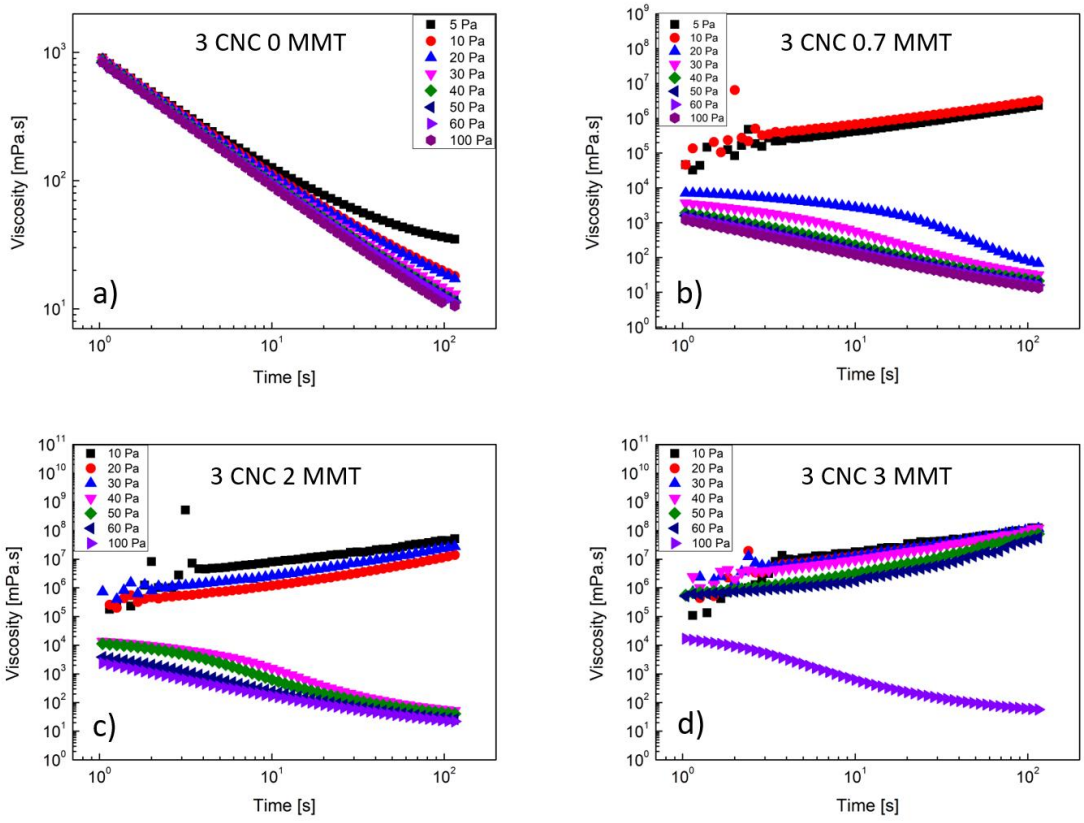

Fig. 5. Creep tests on 3 w/v% CNC with a) 0 b) 0.7 c) 2 and d) 3 w/v% MMT with varying shear stress ranging from 5 to 100 Pa.

Table 2

Yield stress obtained for 3 w/v% CNC at different concentrations of MMT by creep tests.

Sample	Yield stress range
3 CNC 0 MMT	< 5 Pa

3 CNC 0.3 MMT	
3 CNC 0.7 MMT	10-20 Pa
3 CNC 2 MMT	30-40 Pa
3 CNC 3 MMT	60-100 Pa

Three interval thixotropy test (3ITT) is used to ascertain the microstructural restructuring and deformation occurring in CNC/MMT binary mixtures [72,75,76]. A constant shear rate of 1 s^{-1} is applied during the first and third intervals and 100 s^{-1} and 1000 s^{-1} are applied during the second interval and the corresponding viscosity is measured and is plotted as a function of time and is shown in Fig. 6 a) and b) respectively. Viscosity drops suddenly to lower values as the higher shear rate of 100 s^{-1} and 1000 s^{-1} is applied during the second interval and is recovered as the higher shear rates are removed. The recovery degree equation (Eq. 4) is used to determine the sample's structural recovery after a higher shear rate is removed. The recovery viscosity and initial viscosity are represented by η_1 and η_0, respectively [76]. η_0 is measured at 60 s and η_1 is measured at both 85 s and 125 s and the recovery degree of the samples is calculated. The rate of viscosity recovery percentage was reported by Fazilati et al. and is in the range of 42-194 % for pristine CNC suspensions in the concentration range of 4-8 wt% [72]. The anhydrous form of Kaolinite clay, metakaolin was added to calcium sulfoaluminate cement composites to improve the thixotropy behaviour and the viscosity recovery degree was in the 66-74 % as the concentration of Metakaolin increases from 0-3 wt% [76]. The recovery degree of the CNC/MMT binary mixtures is shown in Table S2 and the plot of the recovery degree of the samples with concentration at different times is shown in SI (Fig. S7). The samples recovery degree is in between 55-65% and 25-45% for shear rates 100 s^{-1} and 1000 s^{-1} respectively as MMT is added to CNC aqueous suspensions, which shows slow ageing of the composites.

$$R = \frac{\eta_1}{\eta_0} \text{ x } 100\% \qquad (4)$$

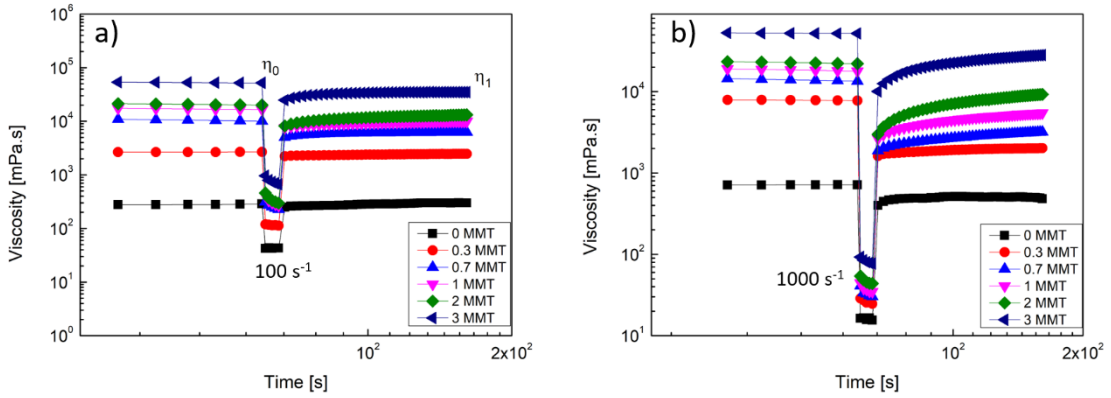

Fig. 6. Three interval thixotropy test (3ITT) of 3 w/v% CNC at a shear rate of a) 100 s^{-1} and b) 1000 s^{-1} with varying concentrations of MMT.

3.4. Large amplitude oscillatory shear (LAOS) measurements

The polymeric materials used for biological and industrial applications have to undergo rapid deformations during their processing. The linear oscillatory shear tests (SAOS) used for measuring the viscoelastic properties of samples would be inadequate in this context and need nonlinear tests (LAOS) to simulate the large deformations on these materials [21]. The nonlinear region is divided into two, the middle amplitude oscillatory shear (MAOS) and LAOS region where the strain amplitude of MAOS ranges from 10% to 100% [22]. Different methods are available nowadays to interpret LAOS data both qualitatively and quantitatively. Lissajous-Bowditch plots, FT-Rheology-stress decomposition methods and Chebyshev polynomials are some of the methods available to analyse the nonlinear viscoelastic properties of the system.

The linear rheological measurements showed the existence of isotropic phase of pristine 3 w/v% CNC suspensions and the presence of liquid crystalline phases on the addition of MMT particles to CNC aqueous suspensions. But only LAOS studies provided in detail which LC phase (nematic or chiral LC) is present at a particular concentration of the sample and discussed about the microstructural changes happening to the system at higher deformations which cannot be provided by linear rheological measurements. The instantaneous stress versus strain plots at different strain amplitudes carried out to observe the network structure response followed by the system at different loading cycles of oscillatory shear tests are usually called as Lissajous-Bowditch (LB) plots [47]. These are actually a visual

representation of the linear to nonlinear transition of the system at higher deformations. LB plots show a straight line for purely elastic materials and a circular shape for perfect viscous materials in their elastic projection and vice versa in their viscous projection [62,63]. The response of a viscoelastic material is in between a straight line and a circular shape. Usually at lower strain amplitudes, the viscoelastic materials exhibit an ellipsoidal shape and a distorted ellipsoidal shape indicates a transition from linear to nonlinear region and the appearance of higher odd harmonics at higher deformations [46,62–64]. The area of the stress vs strain loops (LB plots) is a measure of the dissipated energy of the system. LB plots obtained from stress-strain data analysed using the MITlaos framework of 3 w/v% CNC with varying concentrations of MMT are shown in Fig. 7 and Fig. 8.

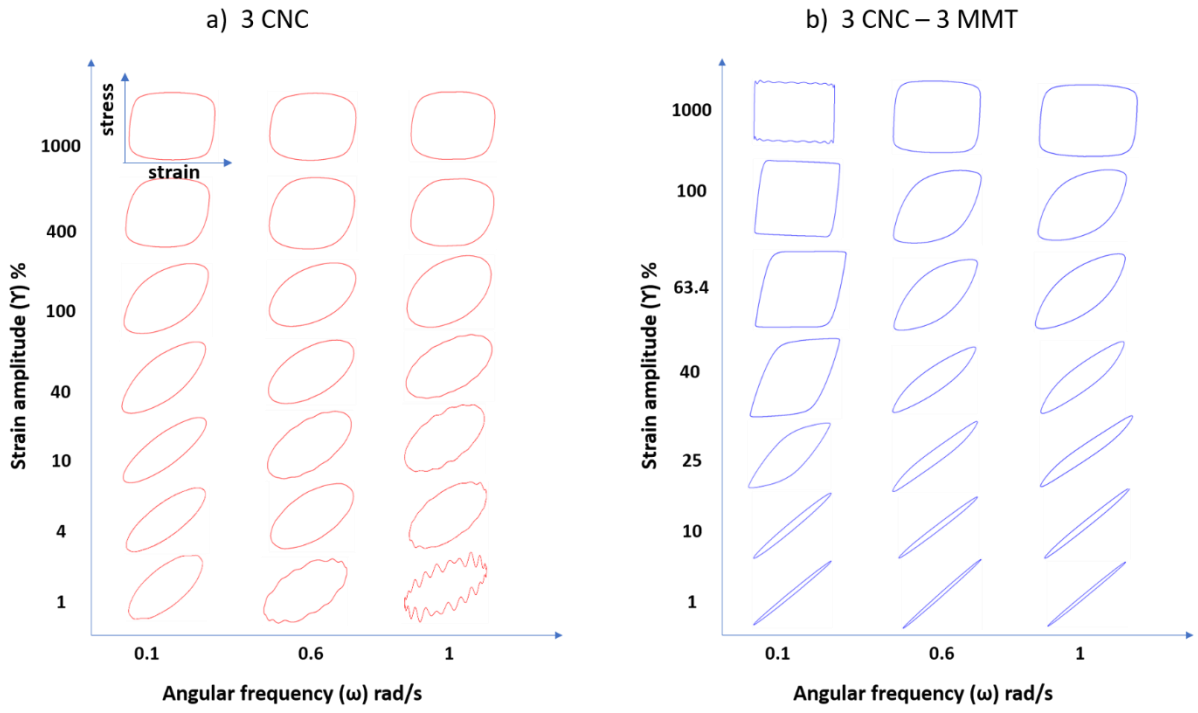

Fig. 7. Elastic LB plots of a) 3 w/v% CNC and b) 3 w/v% CNC with 3 w/v% MMT arranged in the order of increasing ω values from 0.1 to 1 rad/s.

Due to the ellipsoidal shapes that both 3 CNC and 3 CNC 3 MMT exhibit in the elastic LB plots at lower strains—a sign of the linear region—the output stress signal is solely dependent on the fundamental intensity (first harmonic coefficients) of the Fourier series. Higher strain amplitudes distort the ellipse shape and produce a curvilinear parallelogram shape, which is indicative of the sample's nonlinearity and results from the output stress signal's dependence on the higher odd harmonics in the Fourier series expansion [47]. In the linear viscoelastic

(LVE) region, the ellipse shape in the case of 3 CNC 3 MMT is narrower than in the pristine CNC suspension, indicating that adding MMT to CNC aqueous suspensions improves the gelation of the CNC/MMT composite system. [46,65].

In the viscous projection of LB plots, the ellipses are much wider at lower strains which indicates the elastic dominant response of the suspension in the LVE region. At ω=0.1 rad/s, the viscous projection of LB plots exhibits self-intersection loops at higher strain amplitudes and this could be considered as an overshoot in the shear stress response due to the network rupture occurring at higher deformations. The narrowing of the ellipsoidal shapes in the viscous projection and the broadening of these shapes in the elastic projection at higher deformations confirms the network rupture and the liquid-like flow behaviour exhibited by the suspensions in the non-LVE regions. Above a strain of γ_0 = 40% (at ω = 0.1 rad/s) in the elastic LB plots, from a point of zero stress, a linear increase in stress could be observed with an increase in strain which indicates the elastic behaviour of the suspension.

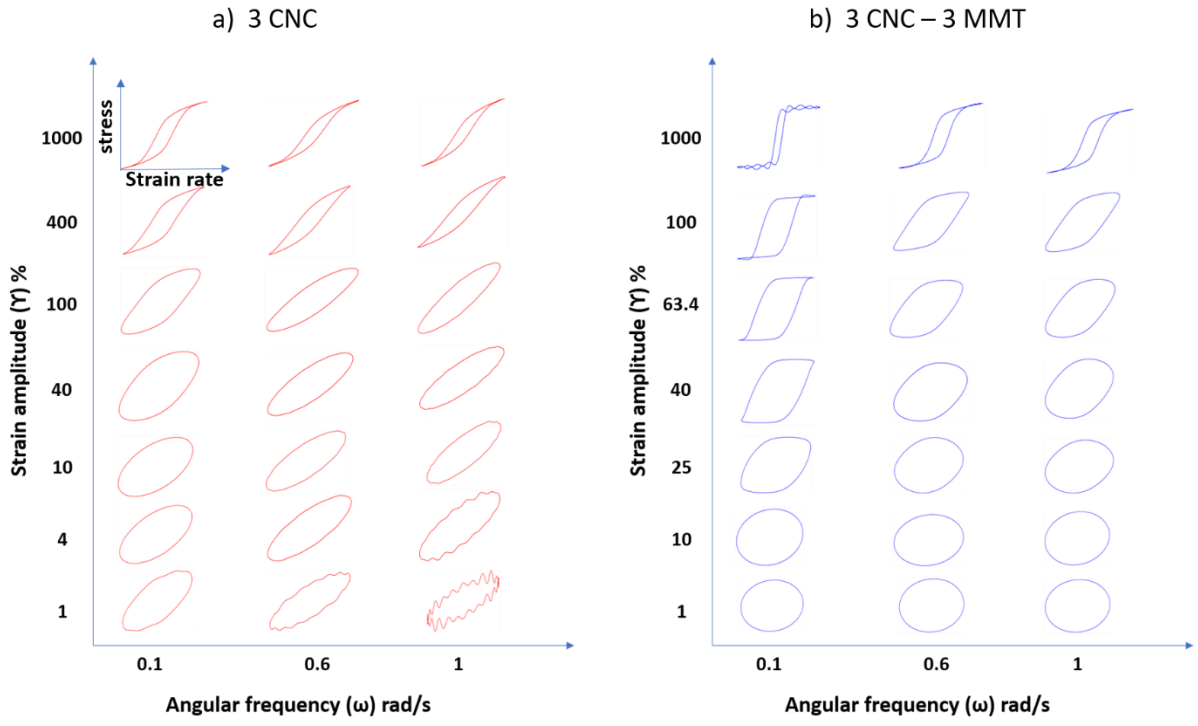

Fig. 8. Viscous LB plots of a) 3 w/v% CNC and b) 3 w/v% CNC with 3 w/v% MMT arranged in the order of increasing ω values from 0.1 to 1 rad/s.

At a certain strain amplitude, the stress value reaches a local maximum (yield stress) and then it slightly decreases and then becomes almost constant (plateau region) as the strain

amplitude increases which indicates the yielding of the sample followed by a decrease in stress values indicating the rupture of the network formed between the particles [77]. The flow of the sample continues as the shear strain increases till it reaches the point of maximum deformation where the sample starts reforming [78]. Then the cycle reverses and then we could see a regeneration of the network taking place at negative strain values thus completing an intra-cycle in the oscillatory shear tests. The structure recovery of the sample is time-dependent (as we can see from the creep and thixotropic tests from Fig. 5 and 6 respectively) and at higher deformations, the stress accumulation would be more and at a particular time the sample has more stress to relax and hence there is no sign of yield stress at higher strain amplitudes γ_0 = 1000%. So here as there is not enough time for the structural regeneration, the sample loses its viscoelastic character and it behaves more as a viscous fluid. The reason for the absence of secondary or self-intersecting loops in the viscous LB plots at higher frequencies (ω > 0.6 rad/s) is that the relaxation time will be less at higher frequencies and during the time of a particular shear, the sample does not get much time to relax from the stress before the next cycle of strain loading takes place [79]. In the nonlinear regime, the dependence of *G'* on shear strain is evident from the deviation of slopes of elastic stress from a straight line to a curved one. From Fig. 9, it is obvious that the concavity is upward for the elastic stress in the region of γ > 0 (positive domain) which indicates the intra-cycle strain stiffening behaviour exhibited by CNC/MMT binary mixtures in the nonlinear regime. Also, the concavity of viscous stress is downward in the nonlinear region indicating the shear thinning behaviour shown by these samples at higher deformations [63]. Even though Lissajous-Bowditch plots are visual representations of linear to nonlinear transitions happening to the system at higher deformations, they do not provide much quantitative information about the nonlinear behaviour.

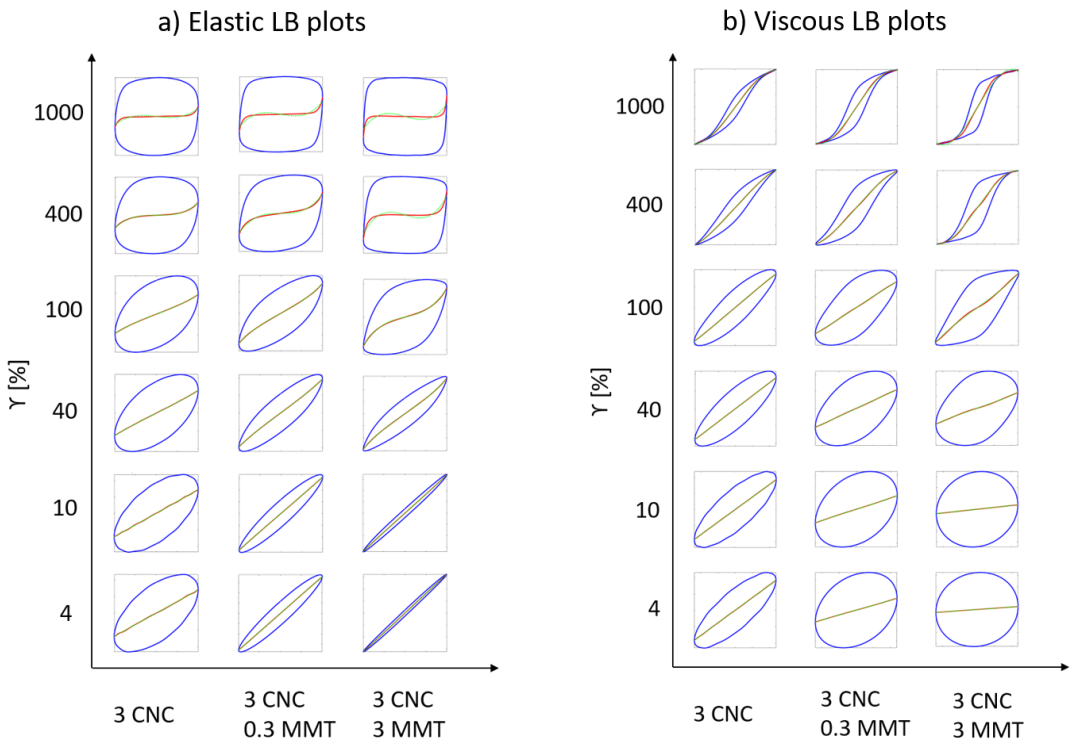

Fig. 9. a) Elastic and b) viscous Lissajous-Bowditch plots with normalized total shear stress (blue solid line) and their corresponding normalized elastic and viscous stresses (red dotted line) obtained using MITlaos framework.

FT-Rheology-stress decomposition methods could serve as a quantitative method available to analyse the nonlinear viscoelastic properties of the system. The purpose of FT rheology is to convert stress signals in the time domain to intensities in the frequency domain where the nonlinearities appear as odd higher harmonics [80]. The output stress response of the LVE region contains only the fundamental intensity contribution of Fourier series expansion in contrast to that of the non-LVE region where higher order odd harmonics terms are also present along with the fundamental intensity values representing the nonlinear regime. The normalised third relative intensities ($I_{3/1}$) are plotted against strain amplitude of 3 w/v% CNC with 0, 0.7, 2 and 3 w/v% of MMT and are shown in Fig. 10. The $I_{3/1}$ vs shear strain plots of 0.3 and 1 w/v% concentrations of MMT added in CNC aqueous suspensions are shown in SI (Fig. S8). For each strain amplitude, three different angular frequencies (ω = 0.1, 0.6 and 1 rad/s) are considered.

In the case of pristine 3 w/v% CNC aqueous suspensions, $I_{3/1}$ values are dependent on angular frequency ω on both MAOS (strain = 10 to 100%) and LAOS (strain = 100 to 1000%) regions and two scaling regions are identified according to the scaling law of $I_{3/1} \alpha \gamma_0^n$. For ω

= 0.1 rad/s, n value is found to be n = 1.41 in the shear strain range of 10 to 25% and n = 0.48 in the range of 40 to 100% and is shown in Fig. 10. For ω = 0.6 rad/s, n value is found to be n = 1.64 in the shear strain range of 15 to 40% and n = 0.82 in the range of 65 to 150% and also in the case of ω = 1 rad/s, n value is found to be n = 1.36 in the shear strain range of 25 to 150%. Thus two scaling regions with a strong ω dependence in the MAOS and LAOS regions indicate the isotropic behaviour of 3 w/v% CNC suspension [46]. The scattered data points at lower deformations could be treated as instrumentation noise produced due to the low torque of the rheometer geometry as a result of the low viscosity of the samples. The slight dependence of $I_{3/1}$ values on ω in the MAOS region and its independency in the LAOS region of 3w/v% CNC with 0.3 and 0.7 w/v% MMT, along with its two scaling regions indicate the biphasic behaviour exhibited by the sample which includes both the isotropic and nematic liquid crystalline phase which is consistent with the literature of pristine CNC systems [46]. For 3 w/v% CNC with 0.3 w/v% MMT, n = 1.15 for the shear strain range of 3 to 7% and n = 0.81 for γ_0 ranging from 10 to 70%. Also, for 3 w/v% CNC with 0.7 w/v% MMT, n = 2 for γ_0 from 7 to 16% and n = 0.99 for γ_0 ranging from 25 to 70% and is shown in Fig. 10.

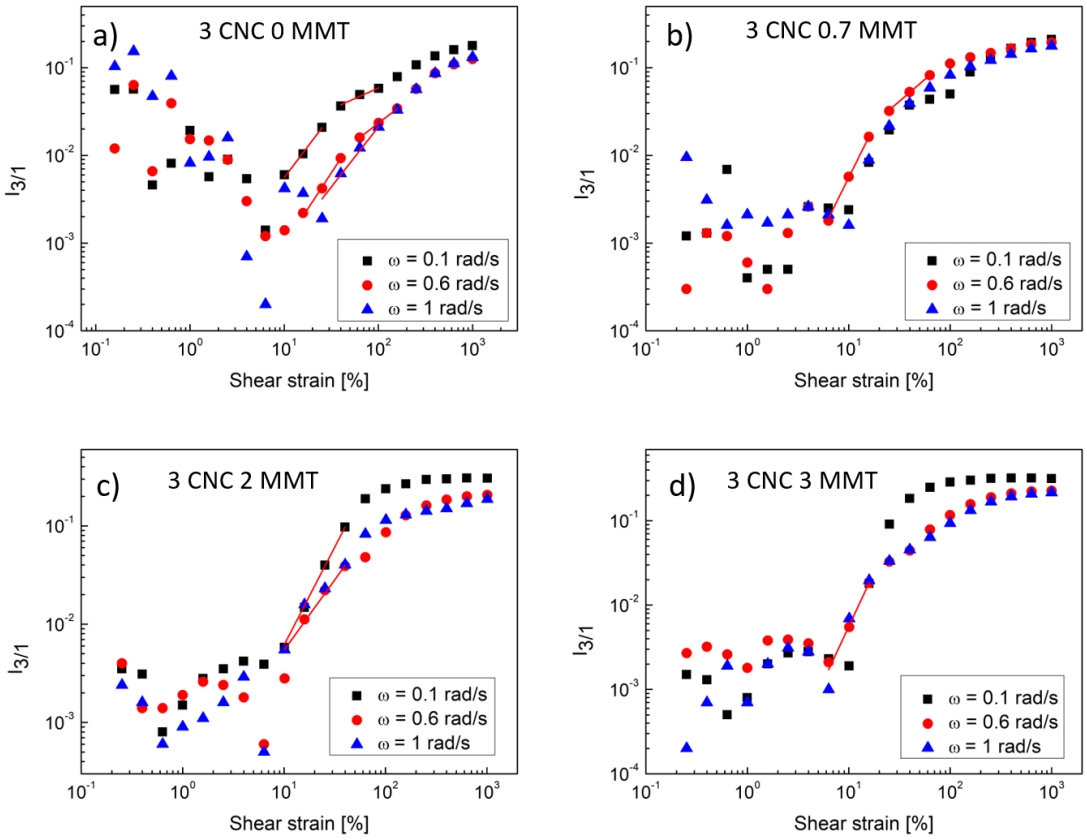

Fig. 10. $I_{3/1}$ vs shear strain plots of 3 w/v% CNC with a) 0 b) 0.7 c) 2 and d) 3 w/v% MMT with different ω values. The red line in the plot is the power law fit of the data points.

The slight dependence of $I_{3/1}$ values on ω in the MAOS region and its large dependence in the LAOS region, in the case of 3 w/v% CNC with 1 and 2 w/v% MMT with multiple scaling regions on the curve indicate the suspensions are biphasic which is consistent with the literature for pristine CNC systems [46]. Since the *n* values are 1.64 and 1.99 respectively for 3 CNC 1 MMT and 3 CNC 2 MMT respectively, in the MAOS region it shows the initiation of chiral nematic LC behaviour exhibited by the suspensions as the *n* values are really close to 2. At a concentration of 3 w/v% CNC with 3 w/v% MMT, $I_{3/1}$ values are nearly independent in the MAOS region and highly dependent in the LAOS region accompanied by a quadratic scaling of $n = 2$ in the MAOS region. This indicates the chiral nematic texture exhibited by this fully birefringent gel, which agrees with the POM images obtained. The ω dependence of the $I_{3/1}$ value could be attributed to the gel formation/percolation threshold. Thus, from LAOS measurements and FT rheology-stress decomposition methods, different phase behaviours exhibited by the CNC/MMT composite suspensions have been revealed.

FT-Rheology analysis method helps to identify the contributions of higher order odd harmonics such as $I_{3/1}$, $I_{5/1}$, $I_{7/1}$, $I_{9/1}$, $I_{11/1}$ etc. The third relative harmonic intensity ($I_{3/1}$) values are often given the utmost importance since they provide major information on the nonlinearities of the system and the higher order harmonics decays fast. The $I_{5/1}$ values of CNC/MMT composite systems are obtained using MITlaos software and are plotted as a function of strain amplitude in Fig. 11. For pristine 3 w/v% CNC, $I_{5/1}$ values are dependent on angular frequency ω on both MAOS (strain = 10 to 100%) and LAOS (strain = 100 to 1000%) regions and two scaling regions are identified according to the scaling law of $I_{5/1}$ α γ_0^n. The *n* values are found to be 1.62 and 0.31 respectively in the shear strain range of 25 to 65 % and 100 to 250% for ω = 0.1 rad/s. For ω = 0.6 rad/s and ω = 1 rad/s, the n values are found to be 0.41 and 1.08 respectively in the shear strain range of 25 to 65 % and n = 0.71 and 0.69 in the shear strain range of 100 to 250 %.

Thus, as in the case of third-order relative harmonic $I_{3/1,}$ here also we could find out two scaling regions with a strong ω dependence in the MAOS and LAOS regions. The $I_{5/1}$ values of 3 w/v% CNC with 0.3 w/v% MMT also exhibit similar behaviour to that of its $I_{3/1}$ values with two scaling regions and a slight dependence of $I_{3/1}$ values on ω in the MAOS region and independence in the LAOS region. The *n* values in the MAOS region of 3 CNC 2 MMT and 3 CNC 3 MMT are 1.46 and 1.97 respectively. The *n* values corresponding to the scaling law of $I_{3/1}$ α γ_0^n and $I_{5/1}$ α γ_0^n are tabulated corresponding to their ω values in Table S3 in SI. Higher order intensity values show a similar trend towards ω values as shown by $I_{3/1}$ values and are not reported elsewhere for CNC/MMT binary mixtures. The $I_{3/1,}$ $I_{5/1,}$ $I_{7/1}$ and $I_{9/1}$ values are compared for a particular value of ω to investigate more on the rapid decay behaviour of higher order odd harmonics and are shown in Fig. 12. There is a decrease in the intensities of higher order odd harmonics for a specific angular frequency value as the n^{th} harmonic value increases [78].

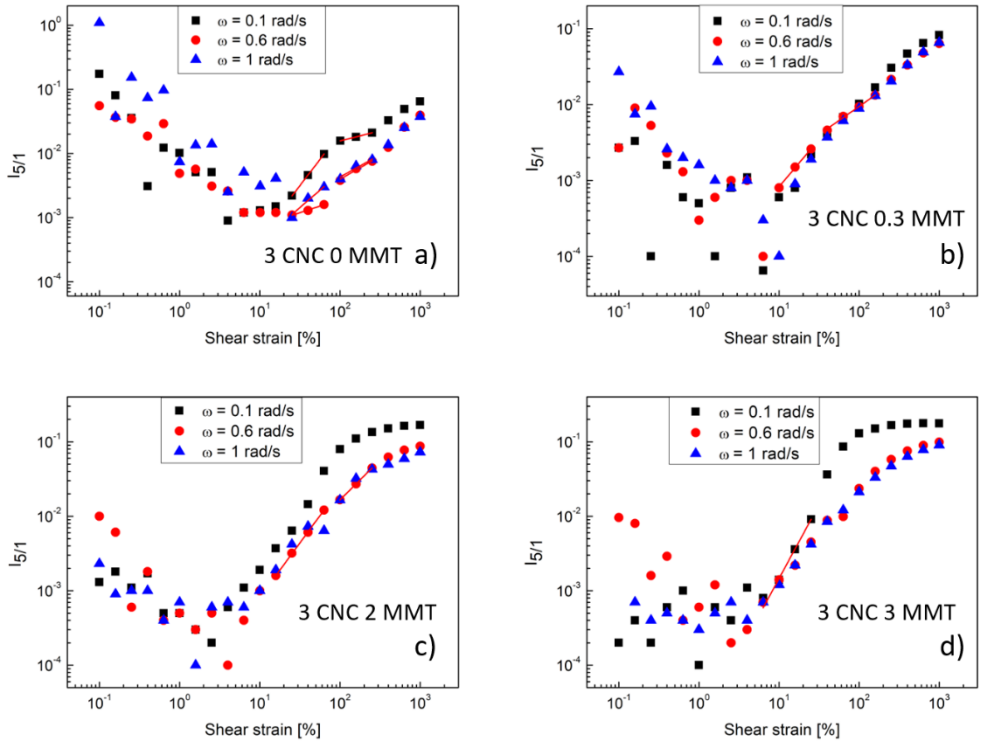

Fig. 11. $I_{5/1}$ vs shear strain plots of 3 w/v% CNC with a) 0 b) 0.3 c) 2 and d) 3 w/v% MMT with different ω values. The red line in the plot is the power law fit of the data points.

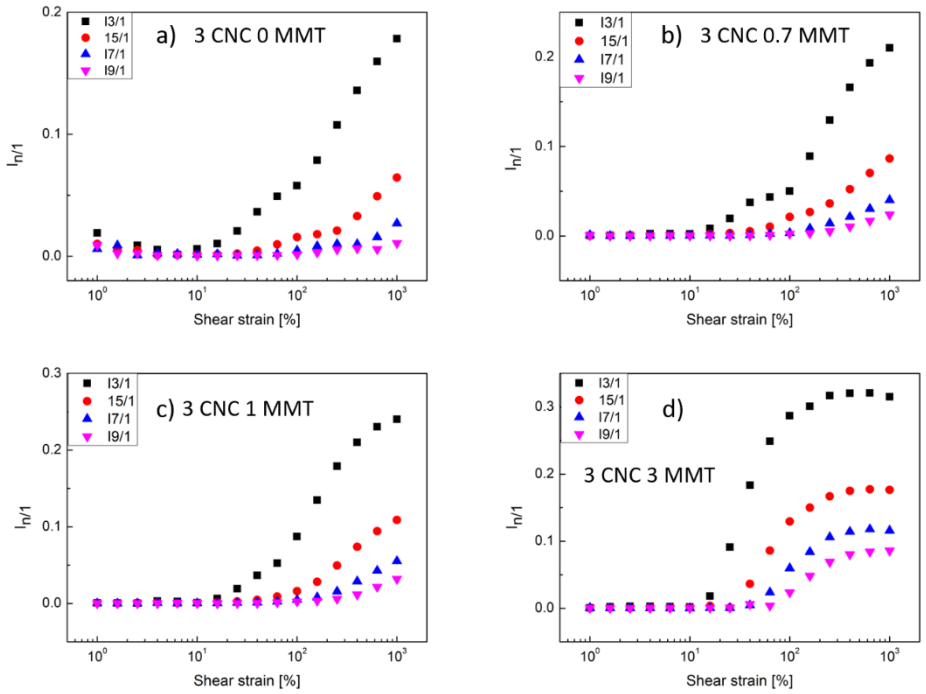

Fig. 12. Normalized higher order odd harmonic intensities ($I_{n/1}$) vs shear strain plots of 3 w/v% CNC with a) 0 b) 0.7 c) 1 and d) 3 w/v% MMT for ω = 0.1 rad/s.

The microstructural changes happening to the system at higher deformations and the intracycle shear thinning/thickening and strain stiffening/softening behaviour of the samples could be investigated using the shear thinning (*S*) and shear thickening (*T*) ratios. At lower deformations, S and T values are zero indicating the linear viscoelastic region. The values of $S > 0$ and $S < 0$ indicate strain stiffening and strain softening behaviours respectively. Similarly, for $T > 0$ and $T < 0$, the values indicate the shear thickening and shear thinning behaviour of the suspensions. Fig. 13 represents the strain stiffening ratio S vs shear strain plots of CNC/MMT composite systems. The scattered data points at lower strain amplitude are due to the instrumentation noise. In the non-LVE region, $S > 0$ for all the suspensions in the investigated range of concentrations which emphasizes the intra-cycle strain stiffening behaviour exhibited by the samples at higher deformations. For pristine 3 w/v% CNC suspensions, S values are ω dependent in both MAOS and LAOS regions indicating its isotropic behaviour. For 3 w/v% CNC 0.1 and 0.7 w/v% MMT, S values are not a function of ω or slightly depending on it, in both MAOS and LAOS region which indicates its biphasic behaviour. In the case of 3 w/v% CNC with 1, 2 and 3 w/v% MMT, S values are ω independent at lower strains (SAOS region) and at very higher strains (LAOS region) and is dependent on the MAOS region which indicates its liquid crystalline behaviour. The large and minimum strain modulus represented by G_L' and G_M' respectively from which S values could be obtained are plotted as a function of shear strain in Fig. S9 (SI). The G_L' and G_M' values are the same in the linear region and it decreases with strain amplitude in the nonlinear regime. The G_M' and G_L' softens at higher strain amplitudes which leads to the apparent strain stiffening behaviour exhibited by the suspensions in MAOS and LAOS region [46]. At lower concentrations of MMT, G_L' and G_M' values are almost independent of ω and the G_L' values decrease with an increase in ω values as the concentration of MMT in CNC aqueous suspension increases.

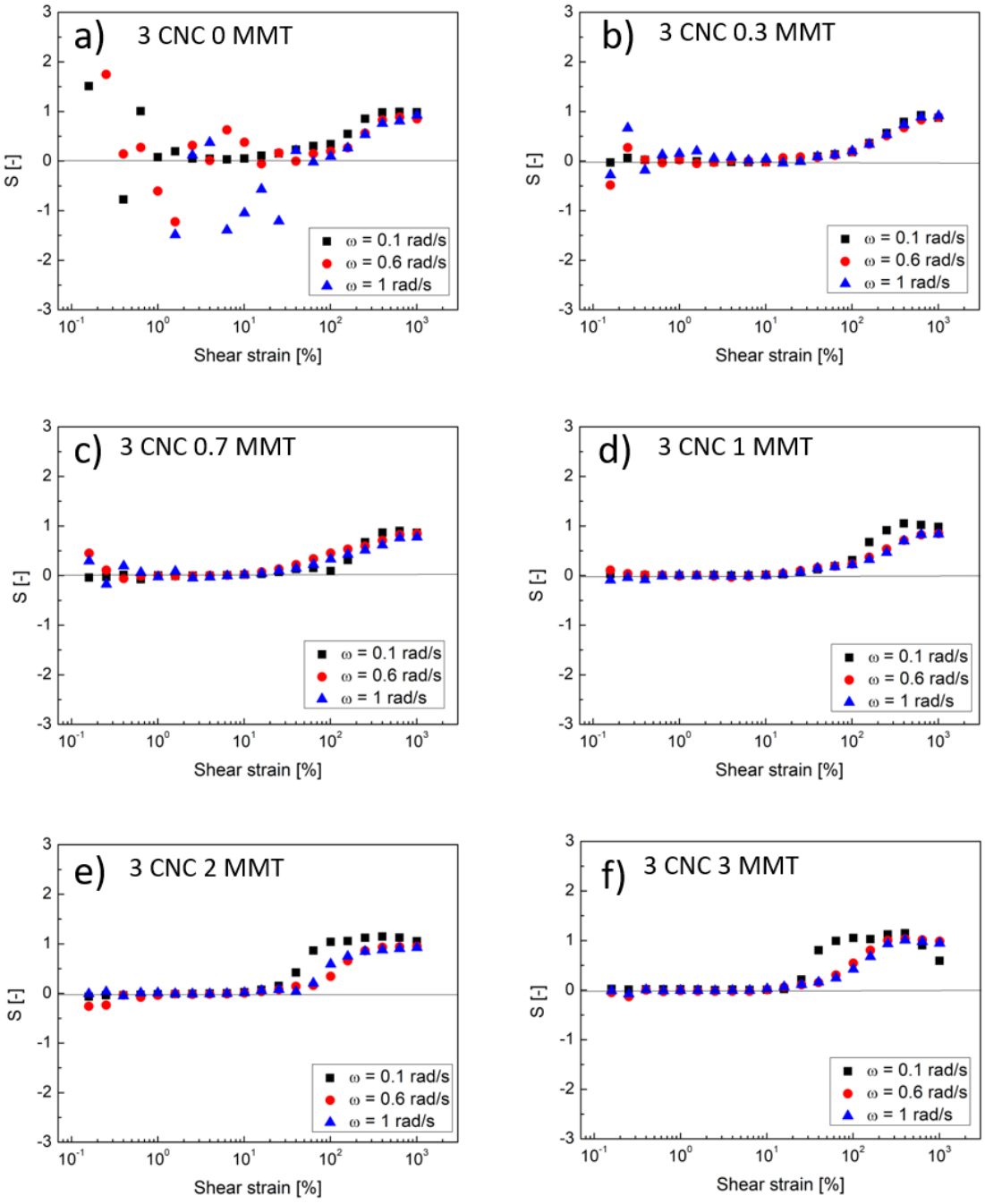

Fig. 13. Strain stiffening ratio (S) vs shear strain of 3 w/v% CNC with a) 0 b) 0.3 c) 0.7 d) 1 e) 2 and f) 3 w/v% MMT.

Shear thickening ratio T is plotted as a function of strain amplitude in Fig. 14. T values are zero at lower deformations for all CNC/MMT suspensions which shows the LVE region. All the suspensions exhibited nonlinear intracycle shear thinning behaviour (T<0) at large strain

amplitudes which may be due to the orientation of particles along the shear direction. At higher concentrations of MMT, a shear thickening behaviour (T>0) is observed for samples in the MAOS region and could be due to the jamming of the gel structure. At MAOS and LAOS regions of pristine 3 w/v% CNC, shear thickening ratio T values are independent of ω and T=0 at the MAOS region and T<0 at the LAOS region which indicates the isotropic behaviour exhibited by this suspension. For 3 w/v% CNC with 0.1 and 0.3 w/v% MMT, T values are not a function of ω and T<0 at higher deformations indicating the biphasic behaviour of these samples. At higher concentrations of MMT, in the MAOS region T values are independent of ω (except in ω =0.1 rad/s for 3 CNC 3 MMT) and a large shift in T value above zero could be observed in the MAOS region and T<0 at LAOS region and the T values are a function of ω which shows the liquid crystalline phase exhibited by these suspensions [46].

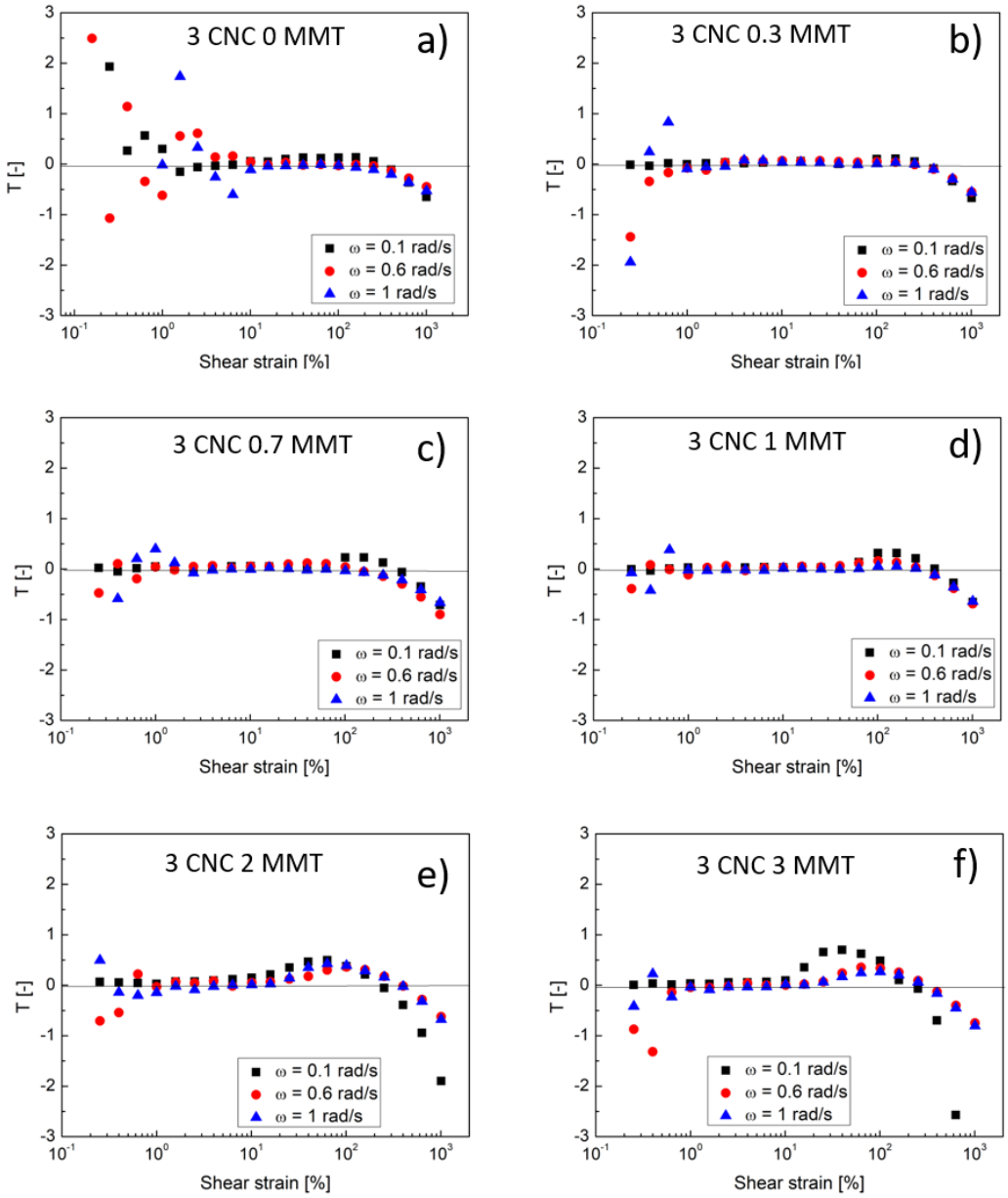

Fig. 14. Shear thickening ratio (T) vs shear strain of 3 w/v% CNC with a) 0 b) 0.3 c) 0.7 d) 1 e) 2 and f) 3 w/v% MMT.

According to Wojno et al. [46] pristine CNC suspensions exhibit LC behaviour at higher concentrations (C > 5 w/v%). However, when MMT, an inorganic clay material, is added to an isotropic 3 w/v% CNC suspension, the resulting CNC/MMT composite suspensions showed LC behavior at lower CNC concentrations. This might be because of the CNC suspensions' MMT-induced self-assembly behavior. Given that CNC nanorods are negatively charged and MMT has positively charged edges, there may be an electrostatic attraction that draws MMT and CNC particles closer together. Additionally, the hydroxyl groups on CNC

may interact with MMT through hydrogen bonding, causing CNC particles to self-assemble and display a range of phase behaviors. We were able to distinguish between the biphasic and isotropic behaviors based on linear rheological measurements. The LAOS measurements showed that the suspensions were fully birefringent gel with chiral nematic liquid crystalline texture at higher concentrations, biphasic at intermediate concentrations, and isotropic at lower concentrations. We hypothesize that 3 CNC with 0 MMT will behave as an isotropic liquid, while 3 CNC with 0.3 and 0.7 MMT will behave as a biphasic system (i.e., both nematic and isotropic liquid behavior). Furthermore, biphasic (isotropic and chiral nematic LC) behavior is displayed by 3 CNC with 1 and 2 MMT and fully birefringent gel with chiral nematic LC texture is displayed by 3 CNC with 3 MMT.

4. Conclusion

To conclude, this study used polarizing microscopy, large amplitude oscillatory shear measurements, and X-ray scattering to examine the phase behaviors of complex colloidal systems of 1D and 2D mixtures. In this work, we used LAOS analysis to identify different phases in cellulose nanocrystal/Montmorillonite systems, such as isotropic, biphasic, or liquid crystalline phases. The CNC-MMT suspensions' intra-cycle nonlinearities, such as strain softening/stiffening and shear thickening/thinning behavior, can be identified with the help of the MITlaos framework, which facilitates the analysis of LAOS data. Lissajous-Bowditch plots, Fourier-transform (FT) rheology, and stress decomposition techniques are also utilized to analyze the nonlinear data in a qualitative and quantitative manner in order to determine the phases that the suspensions at different concentrations displayed. The presence of liquid crystalline phases above 1 w/v% MMT loading to CNC suspensions was confirmed by the three-region viscosity profile and the weak strain overshoot behavior in the amplitude sweep measurements. Both the clear fingerprint texture obtained in the case of 3 w/v% MMT in CNC suspensions and the completely dark background of pristine 3 w/v% CNC suspension without any birefringence in the POM image indicated a transition from an isotropic to a chiral nematic LC phase formation. The linear to nonlinear transition of the composite systems at larger deformations can be seen visually with LB plots.

The dependence of the $I_{3/1}$ value on ω, the multiple scaling regions, and the quadratic scaling regions found in the MAOS region may shed some light on how nonlinear parameters relate to the various phases of CNC/MMT composite systems that are formed. Furthermore, it is clear that all of the suspensions showed shear thinning and nonlinear intra-cycle strain

stiffening behaviours at higher strain amplitudes, indicating that the CNC/MMT composite system is a good choice for coating and paint formulation. These suspensions' strain stiffening behaviours prevents sagging and ensures uniform coverage on vertical surfaces, while their shear thinning behaviour makes application simple and encourages even coating distribution. By utilizing their shear thinning and strain stiffening behaviours, better methods and tools can be developed for handling and processing suspensions.

Acknowledgements

RKP acknowledges the Department of Science and Technology for an INSPIRE Faculty Award Grant [DST/INSPIRE/04/2016/002370] and the Core Research Grants [CRG/2020/006281, CRG/2021/004759] from SERB, Government of India. RKP also thanks the CNRS for financing his research visit to the LPS. C.T. acknowledges support from the Department of Science and Technology, Government of India for INSPIRE fellowship. The authors acknowledge IISER Tirupati for funding and research facilities.

References

[1] Y. Xu, A.D. Atrens, J.R. Stokes, “liquid, gel and soft glass” phase transitions and rheology of nanocrystalline cellulose suspensions as a function of concentration and salinity, Soft Matter. 14 (2018) 1953–1963. https://doi.org/10.1039/c7sm02470c.

[2] D. Bonn, H. Kellay, H. Tanaka, G. Wegdam, J. Meunier, Laponite : What Is the Difference between a Gel and a Glass ?, Langmuir. 22 (1999) 7534–7536. https://doi.org/10.1021/la990167.

[3] C. Tom, V.M.S.G. Tanuku, E. Paineau, R.K. Pujala, Binary Mixtures of Colloidal Cellulose Nanocrystals and Laponite for Preparation of Functional Nanocomposites, ACS Appl. Nano Mater. 4 (2021) 8586–8599. https://doi.org/10.1021/acsanm.1c02210.

[4] E. Sharifzadeh, K. Cheraghi, Temperature-affected mechanical properties of polymer nanocomposites from glassy-state to glass transition temperature, Mech. Mater. 160 (2021) 103990. https://doi.org/10.1016/j.mechmat.2021.103990.

[5] D. Andrienko, Introduction to liquid crystals, J. Mol. Liq. 267 (2018) 520–541.

https://doi.org/10.1016/j.molliq.2018.01.175.

[6] K.M. Herbert, H.E. Fowler, J.M. McCracken, K.R. Schlafmann, J.A. Koch, T.J. White, Synthesis and alignment of liquid crystalline elastomers, Nat. Rev. Mater. 2021 71. 7 (2021) 23–38. https://doi.org/10.1038/s41578-021-00359-z.

[7] K. Ruan, J. Gu, Ordered Alignment of Liquid Crystalline Graphene Fluoride for Significantly Enhancing Thermal Conductivities of Liquid Crystalline Polyimide Composite Films, Macromolecules. 07 (2022) 26. https://doi.org/10.1021/acs.macromol.2c00491.

[8] E. Paineau, A.M. Philippe, K. Antonova, I. Bihannic, P. Davidson, I. Dozov, J. Gabriel, M. Impéror-Clerc, P. Levitz, F. Meneau, L.J. Michot, Liquid–crystalline properties of aqueous suspensions of natural clay nanosheets, Liq. Cryst. Rev. 1 (2013) 110–126. https://doi.org/10.1080/21680396.2013.842130.

[9] F.H. Lin, C. Liu, P. Zhang, On hydrodynamics of viscoelastic fluids, Commun. Pure Appl. Math. 58 (2005) 1437–1471. https://doi.org/10.1002/CPA.20074.

[10] M.K.D. Manshadi, M. Mohammadi, L.K. Monfared, A. Sanati-Nezhad, Manipulation of micro- and nanoparticles in viscoelastic fluid flows within microfluid systems, Biotechnol. Bioeng. 117 (2020) 580–592. https://doi.org/10.1002/BIT.27211.

[11] P. Fischer, E.J. Windhab, Rheology of food materials, Curr. Opin. Colloid Interface Sci. 16 (2011) 36–40. https://doi.org/10.1016/j.cocis.2010.07.003.

[12] H.S. Joyner (Melito), Explaining food texture through rheology, Curr. Opin. Food Sci. 21 (2018) 7–14. https://doi.org/10.1016/j.cofs.2018.04.003.

[13] C. Gallegos, J.M. Franco, Rheology of food, cosmetics and pharmaceuticals, Curr. Opin. Colloid Interface Sci. 4 (1999) 288–293. https://doi.org/10.1016/S1359-0294(99)00003-5.

[14] G. Tafuro, A. Costantini, G. Baratto, S. Francescato, L. Busata, A. Semenzato, Characterization of Polysaccharide Associations for Cosmetic Use: Rheology and Texture Analysis, Cosmet. 8 (2021) 62. https://doi.org/10.3390/cosmetics8030062.

[15] N. Hu, C. Chen, E. Metwalli, L. Bießmann, C. Herold, J. Fu, R. Cubitt, Q. Zhong, P. Müller-Buschbaum, Hydration and Thermal Response Kinetics of a Cross-Linked Thermoresponsive Copolymer Film on a Hydrophobic PAN Substrate Coating Probed

by in Situ Neutron Reflectivity, Langmuir. 37 (2021) 6819–6829. https://doi.org/10.1021/acs.langmuir.1c00931

[16] N. Hu, L. Mi, E. Metwalli, L. Bießmann, C. Herold, R. Cubitt, Q. Zhong, P. Müller-Buschbaum, Effect of Thermal Stimulus on Kinetic Rehydration of Thermoresponsive Poly(diethylene glycol monomethyl ether methacrylate)- block-poly(poly(ethylene glycol) methyl ether methacrylate) Thin Films Probed by In Situ Neutron Reflectivity, Langmuir. 38 (2022) 8094–8103. https://doi.org/10.1021/acs.langmuir.2c00940

[17] X. Zhang, L.P. Kreuzer, D.M. Schwaiger, M. Lu, Z. Mao, R. Cubitt, P. Müller-Buschbaum, Q. Zhong, Abnormal fast dehydration and rehydration of light- And thermo-dual-responsive copolymer films triggered by UV radiation, Soft Matter. 17 (2021) 2603–2613. https://doi.org/10.1039/D0SM02007A.

[18] F. Cherhal, F. Cousin, I. Capron, Influence of charge density and ionic strength on the aggregation process of cellulose nanocrystals in aqueous suspension, as revealed by small-angle neutron scattering, Langmuir. 31 (2015) 5596–5602. https://doi.org/10.1021/acs.langmuir.5b00851

[19] Y. Mao, K. Liu, C. Zhan, L. Geng, B. Chu, B.S. Hsiao, Characterization of Nanocellulose Using Small-Angle Neutron, X-ray, and Dynamic Light Scattering Techniques, J. Phys. Chem. B. 121 (2017) 1340–1351. https://doi.org/10.1021/acs.jpcb.6b11425

[20] F. Azzam, B. Frka-Petesic, E.F. Semeraro, F. Cousin, B. Jean, Small-Angle Neutron Scattering Reveals the Structural Details of Thermosensitive Polymer-Grafted Cellulose Nanocrystal Suspensions, Langmuir. 36 (2020) 8511–8519. https://doi.org/10.1021/acs.langmuir.0c01103

[21] M. Kamkar, R. Salehiyan, T.B. Goudoulas, M. Abbasi, C. Saengow, E. Erfanian, S. Sadeghi, G. Natale, S.A. Rogers, A.J. Giacomin, U. Sundararaj, Large amplitude oscillatory shear flow: Microstructural assessment of polymeric systems, Prog. Polym. Sci. 132 (2022) 101580. https://doi.org/10.1016/j.progpolymsci.2022.101580.

[22] K. Hyun, H.T. Lim, K.H. Ahn, Nonlinear response of polypropylene (PP)/Clay nanocomposites under dynamic oscillatory shear flow, Korea-Australia Rheol. J. 2012 242. 24 (2012) 113–120. https://doi.org/10.1007/S13367-012-0013-2.

[23] K. Hyun, M. Wilhelm, C.O. Klein, K.S. Cho, J.G. Nam, K.H. Ahn, S.J. Lee, R.H. Ewoldt, G.H. McKinley, A review of nonlinear oscillatory shear tests: Analysis and application of large amplitude oscillatory shear (LAOS), Prog. Polym. Sci. 36 (2011) 1697–1753. https://doi.org/10.1016/j.progpolymsci.2011.02.002.

[24] S. Wojno, G. Westman, R. Kadar, Gel point in CNC dispersion from FT Rheology, A. Transactions, T. Nordic, R. Society 27 (2019) 179–184.

[25] X. Li, S.-Q. Wang, X. Wang, Nonlinearity in large amplitude oscillatory shear (LAOS) of different viscoelastic materials, J. Rheol. 53 (2009) 1255. https://doi.org/10.1122/1.3193713.

[26] Merger, Dimitri, Large Amplitude Oscillatory Shear investigations of colloidal systems : experiments and constitutive model predictions, 2015.

[27] J.B. Mirin, L. Kwang, S. Cho, K. Ho, S.D. Kang, Comparison of stress-controlled and strain-controlled rheometers for large amplitude oscillatory shear, (2013) 841–857. https://doi.org/10.1007/s00397-013-0720-8.

[28] M.E.H. Van Den Berg, S. Kuster, E.J. Windhab, L.M.C. Sagis, P. Fischer, Nonlinear shear and dilatational rheology of viscoelastic interfacial layers of cellulose nanocrystals, Phys. Fluids. 30 (2018) 072103. https://doi.org/10.1063/1.5035334.

[29] H. Dai, J. Wu, H. Zhang, Y. Chen, L. Ma, H. Huang, Y. Huang, Y. Zhang, Recent advances on cellulose nanocrystals for Pickering emulsions: Development and challenge, Trends Food Sci. Technol. 102 (2020) 16–29. https://doi.org/10.1016/j.tifs.2020.05.016.

[30] D. Saidane, E. Perrin, F. Cherhal, F. Guellec, I. Capron, Some modification of cellulose nanocrystals for functional Pickering emulsions, Philos. Trans. R. Soc. A Math. Phys. Eng. Sci. 374 (2016). https://doi.org/10.1098/RSTA.2015.0139.

[31] I. Kalashnikova, H. Bizot, B. Cathala, I. Capron, Modulation of cellulose nanocrystals amphiphilic properties to stabilize oil/water interface, Biomacromolecules. 13 (2012) 267–275. https://doi.org/10.1021/BM201599J.

[32] V. Mikulcová, R. Bordes, A. Minařík, V. Kašpárková, Pickering oil-in-water emulsions stabilized by carboxylated cellulose nanocrystals – Effect of the pH, Food Hydrocoll. 80 (2018) 60–67. https://doi.org/10.1016/j.foodhyd.2018.01.034.

[33] W. Du, J. Guo, H. Li, Y. Gao, Heterogeneously Modified Cellulose Nanocrystals-Stabilized Pickering Emulsion: Preparation and Their Template Application for the Creation of PS Microspheres with Amino-Rich Surfaces, ACS Sustain. Chem. Eng. 5 (2017) 7514–7523. https://doi.org/10.1021/acssuschemeng.7b00375

[34] Q.H. Chen, J. Zheng, Y.T. Xu, S.W. Yin, F. Liu, C.H. Tang, Surface modification improves fabrication of pickering high internal phase emulsions stabilized by cellulose nanocrystals, Food Hydrocoll. 75 (2018) 125–130. https://doi.org/10.1016/j.foodhyd.2017.09.005.

[35] X. Li, J. Li, J. Gong, Y. Kuang, L. Mo, T. Song, Cellulose nanocrystals (CNCs) with different crystalline allomorph for oil in water Pickering emulsions., Carbohydr. Polym. 183 (2018) 303–310. https://doi.org/10.1016/j.carbpol2017.12.085.

[36] J. Wu, G.H. Ma, Recent Studies of Pickering Emulsions: Particles Make the Difference, Small. 12 (2016) 4633–4648. https://doi.org/10.1002/SMLL.201600877.

[37] J.F. Revol, H. Bradford, J. Giasson, R.H. Marchessault, D.G. Gray, Helicoidal self-ordering of cellulose microfibrils in aqueous suspension, Int. J. Biol. Macromol. 14 (1992) 170–172. https://doi.org/10.1016/S0141-8130(05)80008-X.

[38] E. Gicquel, J. Bras, C. Rey, J.L. Putaux, F. Pignon, B. Jean, C. Martin, Impact of sonication on the rheological and colloidal properties of highly concentrated cellulose nanocrystal suspensions, Cellulose. 26 (2019) 7619–7634. https://doi.org/10.1007/s10570-019-02622-7.

[39] F. Pignon, M. Challamel, A. De Geyer, M. Elchamaa, E.F. Semeraro, N. Hengl, B. Jean, J.L. Putaux, E. Gicquel, J. Bras, S. Prevost, M. Sztucki, T. Narayanan, H. Djeridi, Breakdown and buildup mechanisms of cellulose nanocrystal suspensions under shear and upon relaxation probed by SAXS and SALS, Carbohydr. Polym. 260 (2021) 117751. https://doi.org/10.1016/j.carbpol.2021.117751.

[40] S. Shafiei-Sabet, W.Y. Hamad, S.G. Hatzikiriakos, Rheology of nanocrystalline cellulose aqueous suspensions, Langmuir. 28 (2012) 17124–17133. https://doi.org/10.1021/la303380v.

[41] S. Shafeiei-Sabet, W.Y. Hamad, S.G. Hatzikiriakos, Influence of degree of sulfation on the rheology of cellulose nanocrystal suspensions, Rheol. Acta. 52 (2013) 741–751.

https://doi.org/10.1007/s00397-013-0722-6.

[42] S. Shafiei-Sabet, W.Y. Hamad, S.G. Hatzikiriakos, Ionic strength effects on the microstructure and shear rheology of cellulose nanocrystal suspensions, Cellulose. 21 (2014) 3347–3359. https://doi.org/10.1007/s10570-014-0407-z.

[43] E.E. Ureña-Benavides, G. Ao, V.A. Davis, C.L. Kitchens, Rheology and phase behavior of lyotropic cellulose nanocrystal suspensions, Macromolecules. 44 (2011) 8990–8998. https://doi.org/10.1021/ma201649f.

[44] G. Lenfant, M. Heuzey, T.G.M. Van De Ven, P.J. Carreau, A comparative study of ECNC and CNC suspensions : effect of salt on rheological properties, Rheol. Acta. (2016). https://doi.org/10.1007/s00397-016-0979-7.

[45] D. Ranjbar, S.G. Hatzikiriakos, Effect of Ionic Surfactants on the Viscoelastic Properties of Chiral Nematic Cellulose Nanocrystal Suspensions, Langmuir. 36 (2020) 293–301. https://doi.org/10.1021/acs.langmuir.9b03437.

[46] S. Wojno, M. Fazilati, T. Nypelö, G. Westman, R. Kádár, Phase transitions of cellulose nanocrystal suspensions from nonlinear oscillatory shear, Cellulose. 29 (2022) 3655–3673. https://doi.org/10.1007/s10570-022-04474-0.

[47] A.A. Moud, M. Kamkar, A. Sanati-Nezhad, S.H. Hejazi, U. Sundararaj, Viscoelastic properties of poly (vinyl alcohol) hydrogels with cellulose nanocrystals fabricated through sodium chloride addition: Rheological evidence of double network formation, Colloids Surfaces A Physicochem. Eng. Asp. 609 (2021) 125577. https://doi.org/10.1016/j.colsurfa.2020.125577.

[48] A. Abbasi, M. Milad, K. Amir, S.S. Hossein, Nonlinear viscoelastic characterization of charged cellulose nanocrystal network structure in the presence of salt in aqueous media, Cellulose. 0123456789 (2020). https://doi.org/10.1007/s10570-020-03166-x.

[49] J. Yang, J.J. Zhao, F. Xu, R.C. Sun, Revealing strong nanocomposite hydrogels reinforced by cellulose nanocrystals: Insight into morphologies and interactions, ACS Appl. Mater. Interfaces. 5 (2013) 12960–12967. https://doi.org/10.1021/am403669n.

[50] A.A. Moud, M. Kamkar, A. Sanati-Nezhad, S.H. Hejazi, Suspensions and hydrogels of cellulose nanocrystals (CNCs): characterization using microscopy and rheology, Cellul. 2022 297. 29 (2022) 3621–3653. https://doi.org/10.1007/S10570-022-04514-9.

[51] S. Yasin, M. Hussain, Q. Zheng, Y. Song, Large amplitude oscillatory rheology of silica and cellulose nanocrystals filled natural rubber compounds, J. Colloid Interface Sci. 588 (2021) 602–610. https://doi.org/10.1016/j.jcis.2020.10.094.

[52] V.K. Vorobiov, M.P. Sokolova, N. V. Bobrova, V.Y. Elokhovsky, M.A. Smirnov, Rheological properties and 3D-printability of cellulose nanocrystals/deep eutectic solvent electroactive ion gels, Carbohydr. Polym. 290 (2022) 119475. https://doi.org/10.1016/j.carbpol.2022.119475.

[53] M. Kaur, M. Arshad, A. Ullah, In-Situ Nanoreinforced Green Bionanomaterials from Natural Keratin and Montmorillonite (MMT)/Cellulose Nanocrystals (CNC), ACS Sustain. Chem. Eng. 6 (2018) 1977–1987. https://doi.org/10.1021/acssuschemeng.7b03380.

[54] S.Z. Zakuwan, I. Ahmad, Effects of hybridized organically modified montmorillonite and cellulose nanocrystals on rheological properties and thermal stability of K-carrageenan bio-nanocomposite, Nanomaterials. 9 (2019) 1547. https://doi.org/10.3390/nano9111547.

[55] M.C. Li, Q. Wu, T. Lei, C. Mei, X. Xu, S. Lee, J. Gwon, Thermothickening Drilling Fluids Containing Bentonite and Dual-Functionalized Cellulose Nanocrystals, Energy and Fuels. 34 (2020) 8206–8215. https://doi.org/10.1021/acs.energyfuels.0c01192.

[56] E.F. Semeraro, N. Hengl, M. Karrouch, L.J. Michot, E. Paineau, B. Jean, J.L. Putaux, C. Lancelon-Pin, L. Sharpnack, F. Pignon, Layered organization of anisometric cellulose nanocrystals and beidellite clay particles accumulated near the membrane surface during cross-flow ultrafiltration: In situ SAXS and ex situ SEM/WAXD characterization, Colloids Surfaces A Physicochem. Eng. Asp. 584 (2020) 124030. https://doi.org/10.1016/j.colsurfa.2019.124030.

[57] R.K. Pujala, H.B. Bohidar, Slow dynamics and equilibrium gelation in fractionated montmorillonite nanoplatelet dispersions, Colloid Polym. Sci. 297 (2019) 1053–1065. https://doi.org/10.1007/s00396-019-04507-4.

[58] R.K. Pujala, H.B. Bohidar, Microstructure and Aging Dynamics of Fluorescent Nanoclay Co-gels of Laponite and Montmorillonite, (2016). https://arxiv.org/abs/1608.08796v1.

[59] P. Munier, S.E. Hadi, M. Segad, L. Bergström, Rheo-SAXS study of shear-induced orientation and relaxation of cellulose nanocrystal and montmorillonite nanoplatelet dispersions, Soft Matter. 18 (2022) 390–396. https://doi.org/10.1039/D1SM00837D.

[60] C. Tom, S.N. Sangitra, R.K. Pujala, Rheological fingerprinting and applications of cellulose nanocrystal based composites: A review, J. Mol. Liq. 370 (2023) 121011. https://doi.org/10.1016/j.molliq.2022.121011.

[61] R. Salehiyan, Y. Yoo, W.J. Choi, K. Hyun, Characterization of morphologies of compatibilized Polypropylene/ Polystyrene blends with nanoparticles via nonlinear rheological properties from FT-rheology, Macromolecules. 47 (2014) 4066–4076. https://doi.org/10.1021/ma500700e.

[62] R. Salehiyan, K. Hyun, Effect of organoclay on non-linear rheological properties of poly(lactic acid)/poly(caprolactone) blends, Korean J. Chem. Eng. 2013 305. 30 (2013) 1013–1022. https://doi.org/10.1007/S11814-013-0035-6.

[63] M. Kamkar, E. Aliabadian, A. Shayesteh Zeraati, U. Sundararaj, Application of nonlinear rheology to assess the effect of secondary nanofiller on network structure of hybrid polymer nanocomposites, Phys. Fluids. 30 (2018) 023102. https://doi.org/10.1063/1.5018863.

[64] J. John, D. Ray, V.K. Aswal, A.P. Deshpande, S. Varughese, Dissipation and strain-stiffening behavior of pectin–Ca gels under LAOS, Soft Matter. 15 (2019) 6852–6866. https://doi.org/10.1039/C9SM00709A.

[65] A. Ettehadi, M. Tezcan, G. Altun, Rheological behavior of water-clay suspensions under large amplitude oscillatory shear, Rheol. Acta. 59 (2020) 665–683. https://doi.org/10.1007/s00397-020-01221-9.

[66] G. Chu, D. Qu, E. Zussman, Y. Xu, Ice-Assisted Assembly of Liquid Crystalline Cellulose Nanocrystals for Preparing Anisotropic Aerogels with Ordered Structures, Chem. Mater. 29 (2017) 3980–3988. https://doi.org/10.1021/acs.chemmater.7b00361.

[67] J.M. Buffa, U. Casado, V. Mucci, M.I. Aranguren, Cellulose nanocrystals in aqueous suspensions: rheology of lyotropic chiral liquid crystals, Cellulose. 26 (2019) 2317–2332. https://doi.org/10.1007/s10570-019-02278-3.

[68] B. Zakani, D. Grecov, Yield stress analysis of cellulose nanocrystalline gels, Cellulose.

(2020) 1–17. https://doi.org/10.1007/s10570-020-03429-7.

[69] F. Cyriac, P.M. Lugt, R. Bosman, On a New Method to Determine the Yield Stress in Lubricating Grease, Tribol. Trans. 58 (2015) 1021–1030. https://doi.org/10.1080/10402004.2015.1035414.

[70] R. Moucka, M. Sedlacik, A. Ronzova, Rheology of uncured magnetorheological elastomers, J. Phys. Conf. Ser. 1527 (2020). https://doi.org/10.1088/1742-6596/1527/1/012012.

[71] A. Abbasi Moud, J. Poisson, Z.M. Hudson, S.G. Hatzikiriakos, Yield stress and wall slip of kaolinite networks, Phys. Fluids. 33 (2021). https://doi.org/10.1063/5.0050541/1076549.

[72] M. Fazilati, S. Ingelsten, S. Wojno, T. Nypelö, R. Kádár, Thixotropy of cellulose nanocrystal suspensions, J. Rheol. 65 (2021) 1035–1052. https://doi.org/10.1122/8.0000281.

[73] P. Coussot, Q D Nguyen, H T Huynh, D. Bonn, Viscosity bifurcation in thixotropic, yielding fluids, J. Rheol. 46 (2002) 573–589. https://doi.org/10.1122/1.1459447.

[74] P. Moller, A. Fall, V. Chikkadi, D. Derks, D. Bonn, An attempt to categorize yield stress fluid behaviour, Philos. Trans. R. Soc. A Math. Phys. Eng. Sci. 367 (2009) 5139–5155. https://doi.org/10.1098/RSTA.2009.0194.

[75] A. Busch, V. Myrseth, M. Khatibi, P. Skjetne, S. Hovda, S.T. Johansen, Rheological characterization of Polyanionic Cellulose solutions with application to drilling fluids and cuttings transport modeling, Appl. Rheol. 28 (2018) 201825154.

[76] M. Chen, L. Yang, Y. Zheng, Y. Huang, L. Li, P. Zhao, S. Wang, L. Lu, X. Cheng, Yield stress and thixotropy control of 3D-printed calcium sulfoaluminate cement composites with metakaolin related to structural build-up, Constr. Build. Mater. 252 (2020) 119090. https://doi.org/10.1016/j.conbuildmat.2020.119090.

[77] R. Shu, W. Sun, T. Wang, C. Wang, X. Liu, Z. Tong, Linear and nonlinear viscoelasticity of water-in-oil emulsions: Effect of droplet elasticity, Colloids Surfaces A Physicochem. Eng. Asp. 434 (2013) 220–228. https://doi.org/10.1016/j.colsurfa.2013.05.057.

[78] A.J. Sandoval, M. Fernández, O. Sanz, A. Santamaría, E. Penott-Chang, A.J. Müller,

Large amplitude oscillatory shear (LAOS) behavior of chocolates of different compositions, J. Rheol. 66 (2022) 859. https://doi.org/10.1122/8.0000425.

[79] A.R. Jacob, A.P. Deshpande, L. Bouteiller, Large amplitude oscillatory shear of supramolecular materials, J. Nonnewton. Fluid Mech. 206 (2014) 40–56. https://doi.org/10.1016/j.jnnfm.2014.03.001.

[80] S. Lee, M. Kim, H.Y. Song, K. Hyun, Characterization of the Effect of Clay on Morphological Evaluations of PLA/Biodegradable Polymer Blends by FT-Rheology, Macromolecules. 52 (2019) 7904–7919. https://doi.org/10.1021/acs.macromol.9b00800.